



# Cosmic Microwave Background Anisotropies

Wayne Hu<sup>1,2,3</sup> and Scott Dodelson<sup>2,3</sup>

<sup>1</sup>Center for Cosmological Physics, University of Chicago, Chicago, IL 60637

<sup>2</sup>NASA/Fermilab Astrophysics Center, P.O. Box 500, Batavia, IL 60510

<sup>3</sup>Department of Astronomy and Astrophysics, University of Chicago, Chicago, IL 60637

KEYWORDS: background radiation, cosmology, theory, dark matter, early universe

**ABSTRACT:** Cosmic microwave background (CMB) temperature anisotropies have and will continue to revolutionize our understanding of cosmology. The recent discovery of the previously predicted acoustic peaks in the power spectrum has established a working cosmological model: a critical density universe consisting of mainly dark matter and dark energy, which formed its structure through gravitational instability from quantum fluctuations during an inflationary epoch. Future observations should test this model and measure its key cosmological parameters with unprecedented precision. The phenomenology and cosmological implications of the acoustic peaks are developed in detail. Beyond the peaks, the yet to be detected secondary anisotropies and polarization present opportunities to study the physics of inflation and the dark energy. The analysis techniques devised to extract cosmological information from voluminous CMB data sets are outlined, given their increasing importance in experimental cosmology as a whole.

## 1 INTRODUCTION

The field of cosmic microwave background (CMB) anisotropies has dramatically advanced over the last decade (c.f. White et al 1994), especially on its observational front. The observations have turned some of our boldest speculations about our Universe into a working cosmological model: namely, that the Universe is spatially flat, consists mainly of dark matter and dark energy, with the small amount of ordinary matter necessary to explain the light element abundances, and all the rich structure in it formed through gravitational instability from quantum mechanical fluctuations when the Universe was a fraction of a second old. Observations over the coming decade should pin down certain key cosmological parameters with unprecedented accuracy (Knox 1995; Jungman et al 1996; Bond et al 1997; Zaldarriaga et al 1997; Eisenstein et al 1999). These determinations will have profound implications for astrophysics, as well as other disciplines. Particle physicists, for example, will be able to study neutrino masses, theories of inflation impossible to test at accelerators, and the mysterious dark energy or

cosmological constant.

For the twenty eight years between the discovery of the CMB (Penzias & Wilson 1965) and the COBE DMR detection of  $10^{-5}$  fluctuations in its temperature field across the sky (Smoot et al 1992), observers searched for these anisotropies but found none except the dipole induced by our own motion (Smoot et al 1977). They learned the hard way that the CMB is remarkably uniform. This is in stark contrast to the matter in the Universe, organized in very non-linear structures like galaxies and clusters. The disparity between the smooth photon distribution and the clumpy matter distribution is due to radiation pressure. Matter inhomogeneities grow due to gravitational instability, but pressure prevents the same process from occurring in the photons. Thus, even though both inhomogeneities in the matter in the Universe and anisotropies in the CMB apparently originated from the same source, these appear very different today.

Since the photon distribution is very uniform, perturbations are small, and linear response theory applies. This is perhaps the most important fact about CMB anisotropies. Since they are linear, predictions can be made as precisely as their sources are specified. If the sources of the anisotropies are also linear fluctuations, anisotropy formation falls in the domain of linear perturbation theory. There are then essentially no phenomenological parameters that need to be introduced to account for non-linearities or gas dynamics or any other of a host of astrophysical processes that typically afflict cosmological observations.

CMB anisotropies in the working cosmological model, which we briefly review in §2, fall almost entirely under linear perturbation theory. The most important observables of the CMB are the power spectra of the temperature and polarization maps. Theory predicts, and now observations confirm, that the temperature power spectrum has a series of peaks and troughs. In §3, we discuss the origin of these acoustic peaks and their cosmological uses. Although they are the most prominent features in the spectrum, and are the focus of the current generation of experiments, future observations will turn to even finer details, potentially revealing the physics at the two opposite ends of time. Some of these are discussed in §4. Finally, the past few years have witnessed important new advances, introduced in §5, from a growing body of CMB data analysts on how best to extract the information contained in CMB data. Some of the fruits of this labor have already spread to other fields of astronomy.

## 2 OBSERVABLES

### 2.1 Standard Cosmological Paradigm

While a review of the standard cosmological paradigm is not our intention (see Narkilar & Padmanabhan 2001 for a critical appraisal), we briefly introduce the observables necessary to parameterize it.

The power spectra shown in Plate I all begin at  $\ell = 2$  and exhibit large errors at low multipoles. The reason is that the predicted power spectrum is the average power in the multipole moment  $\ell$  an observer would see in an ensemble of universes. However a real observer is limited to one Universe and one sky with

the power per logarithmic interval in wavenumber for  $\zeta \ll 1$ . Plate 1 (top) shows observations of  $\Delta T$  along the prediction of the work-ing cosmological model, complete with the acoustic peaks mentioned in §1 and discussed extensively in §3. While COBE first detected anisotropy on the largest scales (inset), observations in the last decade have pushed the frontier to smaller scales (left to right in the figure). The MAP satellite, launched in June 2001, will go out to  $\zeta \sim 1000$ , while the European satellite, Planck, scheduled for launch in 2007, will go a factor of two higher (see Plate 1 bottom).

$$(3) \quad \nabla^2_T \equiv \frac{2\pi}{\ell(\ell+1)} C_{\ell T^2},$$

whose values as a function of  $\ell$  are independent in a given realization. For this reason predictions and analyses are typically performed in harmonic space. On small scales of the sky where its curvature can be neglected, the spherical harmonics analysis becomes ordinary Fourier analysis in two dimensions. In this limit  $\ell$  becomes the Fourier wavenumber. Since the angular wavelength  $\theta = 2\pi/\ell$ , large multipole moments corresponds to small angular scales with  $\ell \sim 10^2$   $\ell$ , whereas the Fourier wavenumber. Likewise, since in this limit the variance represents the scale separations. Likewise, since in this limit the variance of the field is  $\int d^2CC_2(\ell)^2$ , the power spectrum is usually displayed as

$$(2) \quad \langle \Theta_m^* \Theta_n^m \rangle = \langle g_m g_{mm'} C_{i'} \rangle$$

If these fluctuations are Gaussian, then the multipole moments of the temperature field

$$\Theta^{lm} = \int d\mathbf{a} Y_l^m(\mathbf{a}) \Theta(\mathbf{a}) \quad (1)$$

are fully characterized by their power spectrum

## 2.2 CMB Temperature Field

Many of the features of the anisotropies will be produced even if these parameters fall outside the expected range or even if the standard paradigm is incorrect. Where appropriate, we will try to point these out.

For the ordinary matter or baryons,  $\Omega_b \approx 0.02h^{-2}$  ( $w_b \approx 0$ ) with statistical uncertainties at about the ten percent level determined through studies of the light element abundances (for reviews, see Boesgaard & Steigman 1985; Schramm & Turner 1998; Tytler et al 2000). This value is in strikingly good agreement with that implied by the CMB anisotropies themselves as we shall see. There is very strong evidence that there is also substantial mon-baryonic dark matter. This is supported by the fact that there must be a matter of  $\Omega_m \approx 1/3$ . Since the Universe appears to be flat, the total  $\Omega_m$  must be equal to one. Thus, there is a missing component to the matter of  $\Omega_m = -1$  is only one of several possible candidates but we will generally assume this form unless otherwise specified. Measurements of an accelerated expansion from distant supernovae (Riess et al 1998; Perlmutter et al 1999) provide entirely independent evidence for dark energy in this amount.

The initial spectrum of density perturbations is assumed to be a power law with a power law index or tilt of  $n \approx 1$  corresponding to a scale-invariant spectrum. Likewise the initial spectrum of gravitational waves is assumed to be scale-invariant, with an amplitude parameterized by the energy scale of inflation  $E$ , and constrained to be small compared with the initial density spectrum. Finally the formation of structure will eventually reionize the Universe at some redshift

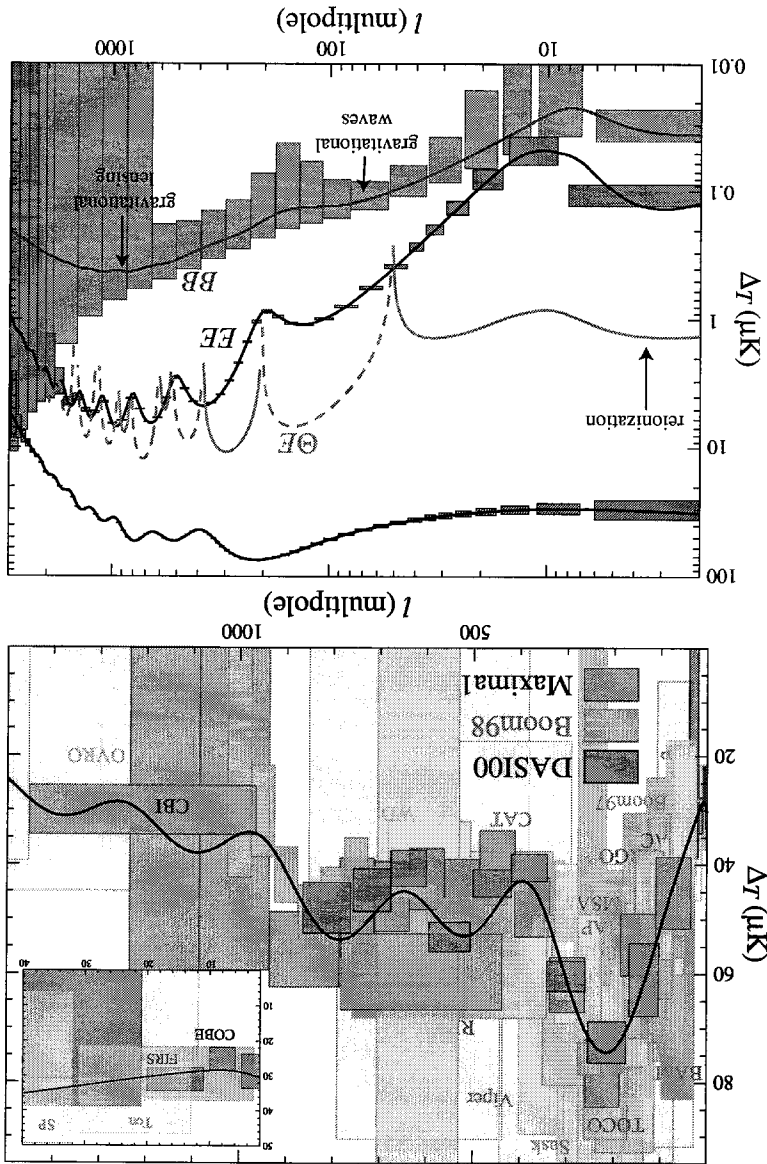
The expansion of the Universe is described by the scale factor  $a(t)$ , set to unity today, and by the current expansion rate, the Hubble constant  $H_0 = 100$  km sec $^{-1}$  Mpc $^{-1}$ , with  $h \approx 0.7$  (Freedman et al 2001). The Universe is flat (no spatial curvature) if the total density is equal to the critical density,  $\rho_c = 1.88 \times 10^{-29}$  g cm $^{-3}$ ; it is open (negative curvature) if the density is less than this and closed by positive curvature if greater. The mean densities of different components of the Universe control  $a(t)$  and are typically expressed today in units of the critical density  $\Omega_i$ , with an evolution with time specified by equations of state  $w_i = p_i/\rho_i$ , where  $p_i$  is the pressure of the  $i$ th component. Density fluctuations are determined by these parameters through the gravitational instability of an initial spectrum of fluctuations.

The working cosmological model contains photons, neutrinos, baryons, cold dark matter and dark energy with densities prescribed within a relatively tight range. For the radiation,  $\Omega_r = 4.17 \times 10^{-5} h^{-2}$  ( $w_r = 1/3$ ). The photon contribution to the radiation is determined to high precision by the measured CMB temperature,  $T = 2.728 \pm 0.004$ K (Fixsen et al 1996). The neutrino contribution follows from the assumption of 3 neutrino species, a standard thermal history, and a negligible mass  $m_\nu$ .  $\ll 1$ eV. Massive neutrinos have an equation of state  $w_\nu = 1/3 \rightarrow 0$  as the particles become non-relativistic. For  $m_\nu \sim 1$ eV this occurs at  $a \sim 10^{-3}$  and can leave a small but potentially measurable effect on the CMB.

Plate I: Top: temperature anisotropy data with boxes representing  $\ell$ - $a$  errors and approximate  $\ell$ -bandwidth. Bottom: temperature and polarization spectra for  $\Omega_0 = 1$ ,  $\Omega_a = 2/3$ ,  $\Omega_b = 0.02$ ,  $\Omega_m h^2 = 0.16$ ,  $n = 1$ ,  $z_1 = 7$ ,  $E_i = 2.2 \times 10^{16}$  GeV. Dashed lines represent negative cross-correlation and boxes represent the statistical errors of the Planck satellite.

While no polarization has yet been detected, general considerations of Thomson scattering suggest that up to 10% of the antiisotropies at a given scale are polarized. Experiments are currently hot on the trail, with upper limits approaching

### 2.3 CMB Polarization Field



Hu & Dodelson

9

5

CMB Anisotropies

The expected level (Hedman et al 2001; Keating et al 2001). Thus, we expect polarization to be an extremely exciting field of study in the coming decade.

The polarization field can be analyzed in a way very similar to the temperature field, save for one complication. In addition to its strength, polarization also has an orientation, depending on relative strength of two linear polarizations states. While classical literature has tended to describe polarization locally in terms of Stokes parameters  $Q$  and  $U$ , recently cosmologists (Seljak 1997; Kamionkowski et al 1997; Zaldarriaga & Seljak 1997) have found that the scalar  $E$  and pseudo-scalar  $B$ , linear but non-local combinations of  $Q$  and  $U$ , provide a more useful description. Postponing the precise definition of  $E$  and  $B$  until §3.7, we can, in complete analogy with Equation (1), decompose each of them in terms of multipole moments, and then, following Equation (2), consider the power spectra,

$$\langle E_m^* E_n^m \rangle = \delta_{mn} C_E, \quad (5)$$

$$\langle B_m^* B_n^m \rangle = \delta_{mn} C_B, \quad (6)$$

$$\langle \Theta_m^* \Theta_n^m \rangle = \delta_{mn} C_\Theta. \quad (7)$$

Both of these features are a direct result of the  $EE$  spectrum being nearly identical to the  $BB$  signal. Indeed, density perturbations do not produce  $B$  modes to first order. A detection of substantial  $B$  polarization, therefore, would be momentous. While  $E$  polarization effectively doubles our cosmological information (while  $E$  polarization effectively doubles our constraints and photons combined to form neutral hydrogen, an event usually known as recombination (Peelbees 1968; Zeldovich et al 1969; see Seager et al 2000 for recent refinements). Before this epoch, free electrons acted as glue between the photons and the baryons through Thomson and Coulomb scattering, so the  $V$ , but this is absent in cosmological settings.

When the temperature of the Universe was  $\sim 3000K$  at a redshift  $z^* \approx 10^3$ , electrons and protons combined to form neutral hydrogen, an event usually known as recombination (Peelbees 1968; Zeldovich et al 1969; see Seager et al 2000 for recent refinements). Before this epoch, free electrons acted as glue between the photons and the baryons through Thomson and Coulomb scattering, so the  $V$ , but this is absent in cosmological settings.

### 3 ACOUSTIC PEAKS

push us qualitatively forward into new areas of physics.

Therefore, while  $E$  polarization effectively doubles our constraints and photons combined to form neutral hydrogen, an event usually known as recombination (Peelbees 1968; Zeldovich et al 1969; see Seager et al 2000 for recent refinements). Before this epoch, free electrons acted as glue between the photons and the baryons through Thomson and Coulomb scattering, so the  $V$ , but this is absent in cosmological settings.

The polarization spectrum shown in Plate 1 [bottom, plotted in  $uk$  following Equation (3)] have several notable features. First, the amplitude of the  $EE$  spectrum is indeed down from the temperature spectrum by a factor of ten. Second, the oscillations, only they are apparently out of phase but correlated with each other, are very similar to the  $EE$  spectrum in every detail of the  $EE$  spectrum. Both of these features are a result of the  $EE$  spectrum being nearly identical to the  $BB$  spectrum, and the scalars  $\Theta$  or  $E$  vanishes.

Partly invariance demands that the cross correlation between the pseudoscalar  $B$  and the scalars  $\Theta$  or  $E$  vanishes.

The polarization spectrum shown in Plate 1 [bottom, plotted in  $uk$  following Equation (3)] have several notable features. First, the amplitude of the  $EE$  spectrum is indeed down from the temperature spectrum by a factor of ten. Second,

the oscillations, only they are apparently out of phase but correlated with each other, are very similar to the  $EE$  spectrum in every detail of the  $EE$  spectrum. Both of these features are a result of the  $EE$  spectrum being nearly identical to the  $BB$  spectrum, and the scalars  $\Theta$  or  $E$  vanishes.

Both of these features are a result of the  $EE$  spectrum being nearly identical to the  $BB$  spectrum, and the scalars  $\Theta$  or  $E$  vanishes.

Both of these features are a result of the  $EE$  spectrum being nearly identical to the  $BB$  spectrum, and the scalars  $\Theta$  or  $E$  vanishes.

Both of these features are a result of the  $EE$  spectrum being nearly identical to the  $BB$  spectrum, and the scalars  $\Theta$  or  $E$  vanishes.

Both of these features are a result of the  $EE$  spectrum being nearly identical to the  $BB$  spectrum, and the scalars  $\Theta$  or  $E$  vanishes.

Both of these features are a result of the  $EE$  spectrum being nearly identical to the  $BB$  spectrum, and the scalars  $\Theta$  or  $E$  vanishes.

Both of these features are a result of the  $EE$  spectrum being nearly identical to the  $BB$  spectrum, and the scalars  $\Theta$  or  $E$  vanishes.

Both of these features are a result of the  $EE$  spectrum being nearly identical to the  $BB$  spectrum, and the scalars  $\Theta$  or  $E$  vanishes.

Both of these features are a result of the  $EE$  spectrum being nearly identical to the  $BB$  spectrum, and the scalars  $\Theta$  or  $E$  vanishes.

Both of these features are a result of the  $EE$  spectrum being nearly identical to the  $BB$  spectrum, and the scalars  $\Theta$  or  $E$  vanishes.

Both of these features are a result of the  $EE$  spectrum being nearly identical to the  $BB$  spectrum, and the scalars  $\Theta$  or  $E$  vanishes.

Both of these features are a result of the  $EE$  spectrum being nearly identical to the  $BB$  spectrum, and the scalars  $\Theta$  or  $E$  vanishes.

Both of these features are a result of the  $EE$  spectrum being nearly identical to the  $BB$  spectrum, and the scalars  $\Theta$  or  $E$  vanishes.

Both of these features are a result of the  $EE$  spectrum being nearly identical to the  $BB$  spectrum, and the scalars  $\Theta$  or  $E$  vanishes.

Both of these features are a result of the  $EE$  spectrum being nearly identical to the  $BB$  spectrum, and the scalars  $\Theta$  or  $E$  vanishes.

Both of these features are a result of the  $EE$  spectrum being nearly identical to the  $BB$  spectrum, and the scalars  $\Theta$  or  $E$  vanishes.

Both of these features are a result of the  $EE$  spectrum being nearly identical to the  $BB$  spectrum, and the scalars  $\Theta$  or  $E$  vanishes.

Table 1: CMB experiments shown in Plate 1 and references.

Name	Authors	Journal Reference	Plank
ARGO	Masi S et al. 1993	Ap. J. Lett. 463:L47-L50	http://map.gsfc.gov
ATCA	Subrahmanyam R et al. 2000	MNRAS 315:808-822	http://map.gsfc.gov
BAM	Tucker GS et al. 1997	Ap. J. Lett. 473:L73-L76	http://map.gsfc.gov
BIIMA	Dawson KS et al. 2001	Ap. J. Lett. 553:L1-L4	http://map.gsfc.gov
BOOM97	Mauskopf PD et al. 2000	Ap. J. Lett. 536:L59-L62	http://map.gsfc.gov
CAT99	Baker JC et al. 1999	MNRAS 308:1173-1178	http://map.gsfc.gov
CAT96	Scott PF et al. 1996	Ap. J. Lett. 461:L1-L4	http://map.gsfc.gov
CBI	Padim S et al. 2001	Ap. J. Lett. 549:L1-L5	http://map.gsfc.gov
COBE	Himshaw G, et al. 1996	Ap. J. 464:L17-L20	http://map.gsfc.gov
DASI	Halverson NW et al. 2001	Ap. J. Lett. 509:L77-L80	http://map.gsfc.gov
FIR	Ganga K, et al. 1994	Ap. J. Lett. 432:L15-L18	http://map.gsfc.gov
IACB	Dicker SR et al. 1999	Ap. J. Lett. 309:750-760	http://map.gsfc.gov
MAX	Torbet E et al. 1999	Ap. J. Lett. 521:L79-L82	http://map.gsfc.gov
MAXIMA1	Lee AT et al. 2001	Ap. J. Lett. 468:L81-L84	http://map.gsfc.gov
MSAM	Wilson GW et al. 2000	Ap. J. Lett. 532:57-64	http://map.gsfc.gov
OVR0	Readhead ACS et al. 1989	Ap. J. 346:566-587	http://map.gsfc.gov
PYTH	Platt SR et al. 1997	Ap. J. Lett. 475:L1-L4	http://map.gsfc.gov
RING	Letch EM et al. 2000	Ap. J. 532:37-56	http://map.gsfc.gov
SP94	Gundersen JO, et al. 1995	Ap. J. Lett. 443:L57-L60	http://map.gsfc.gov
SASK	Netterfield CB et al. 1997	Ap. J. Lett. 477:47-66	http://map.gsfc.gov
SUZIE	Schuster J et al. 1991	Ap. J. Lett. 352:L17-L20	http://map.gsfc.gov
TEN	Gutierrez CM, et al. 2000	Ap. J. Lett. 524:L1-L4	http://map.gsfc.gov
TGCO	Miller AD et al. 1999	Ap. J. 484:537-555	http://map.gsfc.gov
VIFER	Peterson JB et al. 2000	Ap. J. Lett. 532:L183-L186	http://map.gsfc.gov
VLA	Partidge RB et al. 1997	Ap. J. 483:38-50	http://map.gsfc.gov
WD	Tucker GS et al. 1993	Ap. J. Lett. 419:L49	http://map.gsfc.gov

horizon. The physical horizon is a times the comoving horizon. Second, the photon fluid velocity here “ $v$ ” has been written as a scalar instead of a vector. In the early universe, only the velocity component parallel to the comoving direction is finite.

This equation for the photon temperature  $\Theta$ , which does indeed look like the familiar continuity equation in Fourier space (derivatives  $\nabla$  become wave numbers  $k$ ), has a number of subtleties hidden in it, due to the cosmological setting.

$$(L) \quad \text{, } \lambda a y \frac{\xi}{I} - = \Theta$$

space quantities will arise.

and omit the subscript 00 on the Fourier amplitude. Since perturbations are very small, the evolution equations are linear, and different Fourier modes evolve independently. Therefore, instead of partial differential equations for a field  $\Theta(x)$ , we have ordinary differential equations for  $\Theta(k)$ . In fact, due to rotational symmetry, all  $\Theta(k)$  for a given  $k$  obey the same equations. Here and in the following sections, we omit the wavenumber argument  $k$  where no confusion with physical quantities, we omit the wavenumber argument  $k$  where no confusion with physical

$$(9) \quad \int_{\frac{d}{dx}e^{\frac{x}{x-k}}\Theta(x-k)}^{(x-k)\Theta(x-k)} = \Theta^{0=m,0=0} = \Theta$$

Buler equation that encapsulates the basic properties of acoustic oscillations. The discussion of acoustic oscillations will take place exclusively in Fourier space. For example, we decompose the monopole of the temperature field into

For pedagogical purposes, let us begin with an idealization of a perfect photon-barayon fluid and neglect the dynamical effects of gravity and the baryons. Perturbations in this perfect fluid can be described by a simple continuity and an energy-momentum tensor:

3.1 Basics

After recombination the photons basically travel freely to us today, so the problem of translating the acoustic inhomogeneities in the photon distribution at recombination to the anisotropy spectrum today is simply one of projection. This projection depends almost completely on one number, the angular diameter distance between us and the surface of last scattering. That number depends on the energy contents of the Universe after recombination through the expansion rate. The hard wavy projection argument of §3.1 is formalized in §3.8, in the process introducing the popular code used to compute anisotropies, CMBFAST. Finally, we discuss the sensitivity of the acoustic peaks to cosmological parameters in §3.9.

Hu & Dodds

The energy contents of the Universe before recombination all leave their distinct signatures on the oscillations as discussed in §3.3-§3.5. In particular, the cold dark matter and baryon signatures have now been seen in the data (Halverson et al 2001; Netterfield et al 2001; Lee et al 2001). The coupling between electrons and photons is not perfect, especially as one approaches the epoch of recombination. As discussed in §3.3, this imperfection leads to damping in the anisotropy spectrum: very small scale inhomogeneities are smoothed out. The damping phenomenon has now been observed by the CBI experiment (Padin et al 2001). Importantly, fluid imperfections also generate linear polarization as covered in §3.7. Because the imperfection is minimal and appears only at small scales, the polarization generated is small and has not been detected to date.

In §3.2, we introduce the initial conditions that apparently are the source of all chimpiness in the Universe. In the context of *ad initio* models, the term "initial perturbations" refers to the physical mechanism that generates the primordial small oscillations in the Universe. In the working cosmological model, this mechanism is inflation and it sets the initial phase of the oscillations to be the same across all Fourier modes. Remarkably, from this one fact alone comes the prediction that there will be peaks and troughs in the amplitude of the oscillations as a function of wavelength. Additionally the inflationary prediction of an approximately scale-invariant spectrum of density fluctuations is testable.

In §3.1, we start from the two basic equations of fluid mechanics and derive the salient characteristics of the antisotropic spectrum: the existence of peaks and troughs; the spacing between adjacent peaks; and the location of the first peak. These properties depend in decreasing order of importance on the initial conditions, the energy contents of the Universe before recombination and those after recombination. Ironically, the observational milestones have been reached in almost the opposite order. Throughout the 1990's constraints on the location of the first peak steadily improved columnating with precise determinations from the TCCO (Miller et al 1999), Boomerang, (de Bernardis et al 2000) and Maxima-1 (Hanany et al 2000) experiments (see Plate 1 top). In the working cosmological model it shows up right where it should be if the present energy density of the Universe is equal to the critical density, i.e. if the Universe is flat. The skeptical should note that the working cosmological model assumes a particular form for the initial conditions and energy contents of the Universe before recombination which we shall see only recently been tested directly (with an as yet much lower level of statistical confidence) with the higher peaks.

$$D = R \sin(d/R). \quad (12)$$

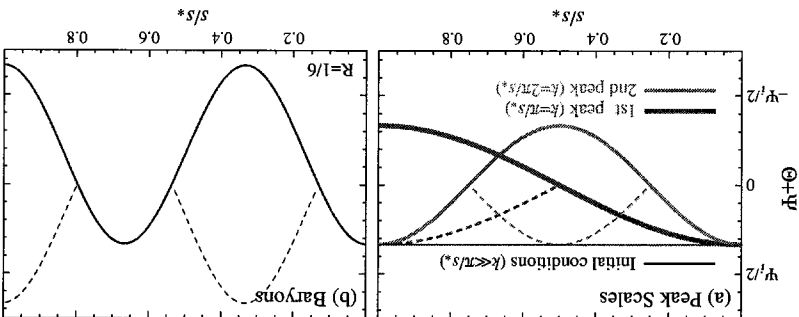
In a spatially curved universe, the angular diameter distance no longer equals the coordinate distance making the peak locations sensitive to the spatial curvature of the Universe (Doroshkevich et al 1978, Kamionkowski et al 1994). Consider first a closed universe with radius of curvature  $R = H_0^{-1}|\Omega_0 - 1|^{1/2}$ . Suppose one spatial coordinate yields a 2-sphere geometry with the observer situated at the pole (see Figure 2). Light travels on lines of longitude. A physical scale  $\lambda$  at fixed latitude given by the polar angle  $\theta$  subtends an angle  $a = \lambda/R \sin \theta$ . For  $a < 1$ , a Euclidean analysis would infer a distance  $D = R \sin \theta$ , even though the coordinate distance along the arc is  $d = \theta R$ , thus

To get a feel for where these features should appear, note that in a flat matter-dominated universe  $\eta \propto (1+z)^{-1/2}$  so that  $\eta/\eta_0 \approx 1/30 \approx 2\%$ . Equivalently  $\eta_1 \approx 200$ . Notice that since we are measuring ratios of distances the absolute scale drops out; we shall see in §3.5 that the Hubble constant sneaks back into the problem because the Universe is not fully matter-dominated at

$$\ell_n \approx n\ell_a, \quad \ell_a \equiv \pi D^*/s^*. \quad (11)$$

the comoving angular diameter distance from the observer to redshift  $z$ . We will address this issue more formally in §3.8. In a flat universe,  $D^* = \eta_0 - \eta^* \approx \eta_0$ , where  $\eta_0 \equiv \eta(z=0)$ . In harmonic space, the relationship implies a coherent series of acoustic peaks in the anisotropy spectrum, located at

**Figure 1:** Idealized acoustic oscillations. (a) Peak scales: the wave mode that completes half an oscillation by recombination sets the physical scale of the first peak. Both minima and maxima correspond to peaks in power (dashed lines, absolute height). Plotted here is the idealization of Equation (16) (constrained multiples of this scale with equal height), and so higher peaks have amplitudes of every other oscillation. Plot here is the idealization of Equation (16) (constraint (16) (constrained multiples of every other oscillation), so by zero loading. (b) Bariton loading. Bariton loading boosts the amplitudes of every other oscillation. Plot here is the idealization of Equation (16) (constraint (16) (constrained multiples of every other oscillation), so by zero loading. (c) Bariton loading. Bariton loading boosts the amplitudes of every other oscillation. Plot here is the idealization of Equation (16) (constraint (16) (constrained multiples of every other oscillation), so by zero loading. (d) Bariton loading. Bariton loading boosts the amplitudes of every other oscillation. Plot here is the idealization of Equation (16) (constraint (16) (constrained multiples of every other oscillation), so by zero loading.



Hu & Dodelson

How does this spectrum of inhomogeneities at recombination appear to us today? Roughly speaking, a spatial inhomogeneity in the CMB temperature of wavelength  $\chi$  appears as an angular anisotropy of scale  $\theta \approx \chi/D$  where  $D(z)$  is

In the limit of scales large compared with the sound horizon  $k_s \ll 1$ , the perturbation is frozen into its initial conditions. This is the first of the statements that the large-scale anisotropies measured by COBE directly measure the initial conditions. On small scales, the amplitude of the Fourier modes will exhibit temporal oscillations, as shown in Figure 1 [with  $\Psi = 0$ ,  $\Psi_i = 3\Theta(0)$  for this idealization]. Modes that are caught at maxima or minima of their oscillation idealization] follow a harmonic relationship  $k_s = n\pi/s$ , where  $n$  is an integer (see Peacock 1991).

$$\Theta(\eta^*) = \Theta(0) \cos(k s^*), \quad (10)$$

where  $c_s \equiv \sqrt{p/\rho} = 1/\sqrt{3}$  is the sound speed in the (dynamically barion-free) fluid. What this equation says is that pressure gradients act as a restoring force to any initial perturbation in the system which thereafter oscillate at the speed of sound. Physically these temperature oscillations represent the heating and cooling of a fluid that is compressed and rarefied by a standing sound wave. This behavior continues until recombination. Assuming negligible initial velocity perturbations, we have a temperature distribution at recombination of

$$(6) \quad c_2^2 k_2^2 \Theta = 0,$$

Differences in fitting the countinuity equation and estimating the Euler equation yields the most basic form of the oscillator equation

$$(8) \quad \cdot \Theta q = \nu_q$$

The Euler equation for a fluid is an expression of momentum conservation, effects of gravity, The Euler equation then becomes

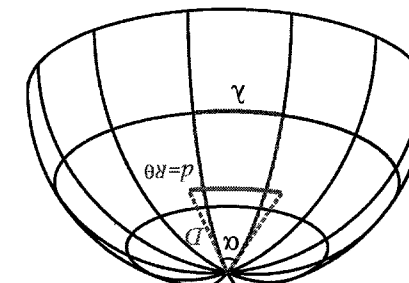
wavevector  $\mathbf{k}$  is expected to be important, since they alone have a source in gravity. Specifically,  $V_\lambda = -i\omega \mathbf{k}$ . In terms of the moments introduced in §2,  $v_\lambda$  represents a dipole moment directed along  $\mathbf{k}$ . The factor of  $1/3$  comes about since continuity conserves photon number not temperature and the number density  $n_\gamma \propto T^3$ . Finally, we emphasize that, for the time being, we are neglecting the

For open universes, simply replace  $\sin$  with  $\sinh$ . The result is that objects in an open (closed) universe are closer (further) than they appear, as it seen through a lens. In fact one way of viewing this effect is as the gravitational lensing due to the background density (c.f. §4.2.4). A given comoving scale at a fixed distance subtends a larger (smaller) angle in a closed (open) universe than a flat universe. This strong scaling with spatial curvature indicates that the observed first peak at  $\ell_1 \approx 200$  constraints the geometry to be nearly spatially flat. We will implicitly assume spatial flatness in the following sections unless otherwise stated.

Finally in a flat dark energy dominated universe, the conformal age of the universe decreases approximately as  $\eta_0 \rightarrow \eta_0(1 + h_0^{0.085})$ . For reasonable  $Q_m$ , this causes only a small shift of  $\ell_1$  to lower multipoles (see Plate 4) relative to the effect of curvature. Combined with the effect of the radiation near recombination, the peak locations provides a means to measure the physical age to of a flat universe (Hu et al 2001).

As suggested above, observations of the location of the first peak strongly point to a flat universe. This is encouraging news for adherents of inflation, a theory which initially predicted  $Q_{\text{tot}} = 1$  at a time when few astrophysicists would sign on to such a high value (see Liddle & Lyth 1993 for a review). However, the argument for inflation goes beyond the confirmation of flatness. In particular, the discussion of the last subsection begs the question: whence  $\Theta(0)$ , the initial conditions of the temperature fluctuations of causality which point to inflation as the origin of the universe?

**Figure 2:** An irregular diameter distance. In a closed universe, objects are further than they appear at larger angles or lower in a closed universe. The converse is true for an open universe.



The results from the idealization of §3.1 carry through with a few exceptions. Even without an initial temperature fluctuation to displace the oscillator, acoustic oscillations would arise by the initial condition of the fluid into gravitational potential wells. Since it is the effective temperature  $\Theta + \frac{1}{2}$  that oscillates, they occur even if  $\Theta(0) = 0$ . The quantity  $\Theta + \frac{1}{2}$  can be thought of as an effective temperature in another way: after recombination, photons must climb out of the potential well to the observer and thus suffer a gravitational redshift of  $\Delta T/T = \frac{1}{2}$ . The effective temperature fluctuation is therefore also the observed temperature fluctuation. We now see that the large scale limit of Equation (15) recovers the famous Schwarzschild result that the observed temperature  $\Theta + \frac{1}{2}$  is  $\frac{1}{3}$  and overdense regions correspond to cold spots on the sky (Sachs & Wolfe 1967). When  $\frac{1}{2} < 0$ , although  $\Theta$  is positive, the effective temperature  $\Theta + \frac{1}{2}$  is negative. The plasma begins effectively rarefied in gravitational potential wells. As gravity compresses the fluid and pressure resists, rarefaction becomes compression and rarefaction again. The first peak corresponds to the mode that is caught in its first compression by recombination. The second peak roughly half the wavelength corresponds to the mode that went through a full cycle of compression and rarefaction by recombination. We will use this language at the end of the paper.

$$\Theta + \Psi [m] = (\Theta + \Psi) [m] \cos(ks) =$$

in the absence of baryons,  $c_2 = 1/3$  so the new oscillator equation is identical to Equation (9) with  $\Theta$  replaced by  $\Theta + \Psi$ . The solution in the matter dominated epoch is then

$$\cdot \frac{3}{k_2^2} = \Theta - c_2^3 k_2^2 \Theta \quad (14)$$

Gravitiy also changes the Newtonian curvature equation. Since the Newtonian curvature equation is essentially a perturbation to the scale factor, changes in its value also generate temperature perturbations by analogy to the cosmological redshift  $\delta\theta = -\phi$  and so the continuity equation (7) gains a contribution of  $-\dot{\phi}$  on the rhs.

We saw above that fluctuations in a scalar field during inflation get turned into temperature fluctuations via the intermediate law of gravity. Gravity affects  $\Theta$  in more ways than this. The Newtonian potential and spatial curvature alter the acoustic oscillations by providing a gravitational force on the oscillator. The Euler equation (8) gains a term on the rhs due to the gradient of the potential  $\Phi$ . The main effect of gravity then is to make the oscillations a competition between pressure gradients  $\Phi$  and potential gradients  $\Phi$  with an equilibrium when  $\Theta + \dot{\Phi} = 0$ .

### 3.3 Gravitational Horizons

Allermate models which seek to obey the causality can generate curvature fluctuations only inside the particle horizon. Because the perturbations are then not generated at the same epoch independent of scale, there is no longer a unique relationship between the phase of the oscillators. That is, the argument of the cosine in Equation (10) becomes  $k_s + \phi(k)$ , where  $\phi$  is a phase which can in principle be different for different wavevectors, even those with the same magnitude  $k$ . This can lead to temporal incoherence in the oscillations and hence a loss of strict regularity of causality since there are other ways to synch up the oscillations. For example, many isocurvature models, where the initial spatial curvature is unperturbed, are coherent since their oscillations begin with the initial separation of curvatures at horizon crossing (Hu & White 1996). Still they typically have  $\phi \neq 0$  (C.L. Turner 1996). Independent of the angular diameter distance  $D^*$ , the ratio of the peak locations gives the phase:  $\ell_1 : \ell_2 : \ell_3 \sim 1 : 2 : 3$  for  $\phi = 0$ . Likewise independent of a constant phase, the spacing of the peaks for  $\phi \neq 0$  gives a measure of the angular diameter distance (Hu & White 1996). The observations, which indicate coherent oscillations with  $\phi = 0$ , therefore provide a non-trivial test of the inflationary paradigm and support a substantially more stringently version of the horizon problem for conformers to  $\ell_n - \ell_{n-1} = \ell$ .

$$\cdot \frac{t}{t\varphi} - \left( \frac{d}{d} + 1 \right) \frac{3}{2} = \frac{v}{v\varphi} - = \Theta$$

In turn depends on time as  $a \propto t^{2/3(1+p)}$ . Therefore, the fractional change in the CMB temperature

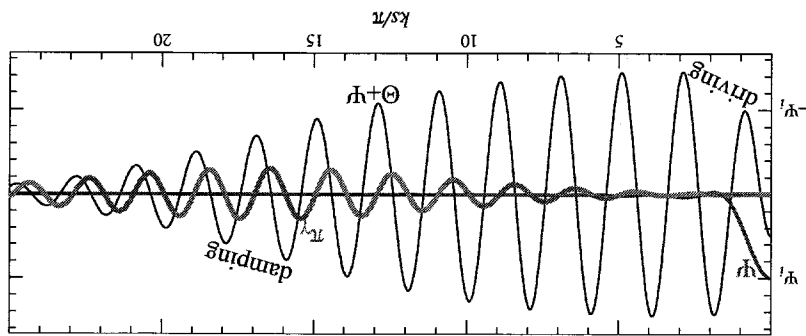
We have hitherto also been neglecting the energy density of the radiation in comparison to the matter. The matter-to-radiation ratio scales as  $p_m/p_r \approx 240m^2h^2(2/10^3)^{-1}$  and so is also of order unity at recombination for reasonable parameters. Moreover fluctuations corresponding to the higher peaks entered the sound horizon at an earlier time, during radiation domination.

Including the radiation changes the expansion rate of the Universe and hence the physical scale of the sound horizon at recombination. It introduces yet another potential ambiguity in the interpretation of the location of the peaks. Fortunately, the matter-radiation ratio has another effect in the power spectrum by which it can be distinguished. Radiation drives the acoustic oscillations by making the gravitational force evolve with time (Hu & Sugiyama 1995). Matter does not.

The exact evolution of the potentials is determined by the relativistic Poisson equation. But qualitatively, we know that the background density is decreasing with time, so unless the density fluctuations in the dominant component grow with time, the density fluctuations will decay. In particular, in the radiation dominated era once pressure gradients to fight gravity at the first comptonized maxima of the wave, the Newtonian gravitational potential curvature must decay (see Figure 3).

### 3.5 Radiation Draining

**Figure 3:** Radiation driving and diffusion damping. The decay of the potential  $\Psi$  drives the oscillation in the radiation dominated epoch. Diffusion generates viscosity  $\eta$ , i.e. a quadrupole moment in the temperature, which damp oscillations and generates polarization. Plotted here is the numerical solution to Equation (18) and Equation (19) for a mode with wavelength much smaller than the sound horizon at decoupling,  $\eta s \ll 1$ .



Hu & Dodelson

Aside from the lowering of the sound speed which decreases the sound horizon, barions have two distinguishing effects: they enhance the amplitude of the oscillations and shift the equilibrium point to  $\Theta = -(1 + R)\Phi$  (see Figure 1b). These two effects are intimately related and are easy to understand since the equations of motion have two variables: the energy density  $\Theta = (1 + R)\Phi$  and the field  $\Phi$ . For the same initial conditions, increasing the mass causes the oscillator to fall further in the gravitational field leading to larger oscillations and a shifted zero point.

The shifting of the zero point of the oscillator has significant phenomenological consequences. Since it is still the effective temperature  $\Theta + \dot{\Phi}$  that is the observed temperature, the zero point shift breaks the symmetry of the oscillations. The barions enhance only the compressional phase, i.e., every other peak. For the working cosmological model these are the first, third, fifth, ... Physically, the extra gravity provided by the barions enhances compression into potential wells. These qualitative results remain true in the presence of a time-variable mass.

An additional effect arises due to the adiabatic damping of an oscillator with a time-variable mass. Since the energy/frequency of an oscillator is an adiabatic invariant, the amplitude must decay as  $(1 + R)^{-1/4}$ . This can also be understood qualitatively. Since the energy/frequency of an oscillator is an adiabatic invariant, the amplitude must decay as  $(1 + R)^{-1/4}$ . This can also be understood qualitatively. Since the energy/frequency of an oscillator is an adiabatic invariant, the amplitude must decay as  $(1 + R)^{-1/4}$ .

$$[\Theta + (I + R)\Phi](\eta^m) \cos(\eta s) = [\Theta + (I + R)\Phi](\eta) \quad (17)$$

Barions are conceptually easy to include in the evolution equations since their momentum density provides extra inertia in the joint Euler equation for pressure and potential gradients to overcome. Since inertial and gravitational mass are equal, all terms in the Euler equation save the pressure gradient are multiplied by  $1 + R$  leading to the revised oscillator equation (Hu & Sugiyama 1995) (16)

$$\frac{c_s}{k^2} \frac{dp}{d\eta} (c_s^2 \Theta) + c_s^2 k^2 \Theta = - \frac{3}{k^2} \Phi - c_s^2 \frac{dp}{d\eta} (c_s^2 \Phi),$$

where we have used the fact that the sound speed is reduced by the barions to  $c_s = 1/\sqrt{3(1+R)}$ . To get a feel for the implications of the barions take the limit of constant  $R$ ,  $\Phi$  and  $\Psi$ . Then  $d^2(R\Psi)/d\eta^2 (= 0)$  may be added to the left hand side to again put the oscillator equation in the form of Equation (9) with  $\Theta \leftarrow \Theta + (1+R)\Psi$ .

The solution then becomes

So far we have been neglecting the baryons in the dynamics of the acoustic oscillations. To see whether this is a reasonable approximation consider the photon-baryon momentum density ratio  $R = (p_b + p_\theta)/(p_\theta + p_\gamma) \approx 30 h^6 (z/10^8)^{-1}$ . For typical values of the baryon density this number is of order unity at recombina-

### 3.4 Baryon Loading

In the photon Euler equation there is an extra force on the rhs due to anisotropic stress gradients or radiation viscosity in the fluid,  $\bar{u}_r$ . The anisotropic stress is directly proportional to the quadrupole moment of the photon temperature distribution. A quadrupole moment is established by gradients in  $\bar{u}_r$ , as photons say negligibly moment is established by gradients in  $\bar{u}_r$ , as photons from say negligibly temperature crests meet at a trough (see Plate 3, inset). However it is destroyed by scattering. Thus  $\bar{u}_r = 2(k\bar{u}_r/\tau)A_r$ , where the order unity constant can be derived from the Boltzmann equation  $A_r = 1/15$  (Kasner 1983). Its evolution is shown in Figure 3. With the continuity Equation (7),  $k\bar{u}_r \approx -3\Theta$  and so viscosity takes the form of a damping term. The heat conduction term can be shown to have a similar effect by expanding the Euler equation in  $k/\tau$ . The final oscillator equation including both terms becomes

$$\frac{\partial}{\partial t} \left( C_s \frac{du}{dr} \right) + \frac{k^2}{C_s} [A_r + C_s \bar{u}_r] = - \frac{3}{k^2} \Phi - C_s \frac{d\eta}{dr} (C_s^{-2} \dot{\Phi}), \quad (20)$$

where the heat conduction coefficient  $A_r = R_r^2/(1+R_r)$ . Thus we expect the inhomogeneities to be damped by a exponential factor of order  $e^{-k^2 r/\tau}$  (see Figure 3). The damping scale  $k\tau$  is thus of order  $\sqrt{\tau}/\eta$ , corresponding to the geometrical mean of the horizon and the mean free path. Damping can be thought of as the result of the random walk in the barions that takes photons from hot regions into cold and vice-versa (Sik 1968). Detailed numerical integration of the equations of motion are required to track the rapid growth of the damping length through recombination itself. These calculations show that the damping length offsets by a decrease in the ionization fraction due to recombination.

The net result under the Shiba approximation is that the damping length scales is partially offset by a decrease in the ionization fraction due to recombination. This is partly density: the increase in electron density is in turn controlled by the free barions is controlled by the mean free path which is in turn controlled by the free electrons is controlled by the slightly less damping at a fixed peak number. The dependence on responses to slighly less damping at a fixed multipole moment; conversely, it corresponds into more inveresly proportional to the expansion rate. Thus, more matter which is also inversely proportional to the expansion rate. The matter density goes up. Since the diffusion length is proportional to  $\sqrt{\tau}$ , it too decreases as matter density  $\Omega_m h^2$  increases, the horizon  $\eta$ , decreases since the expansion rate goes up. Does this suppression depend on the cosmological parameters? As the matter density  $\Omega_m h^2$  increases, the horizon  $\eta$ , decreases since the expansion rate goes up but not as much as the angular diameter distance  $D$ .

How does this suppression depend on the cosmological parameters? As the scale is of order  $k\tau \approx 10$  leading to a substantial suppression of the oscillations beyond the third peak.

$$c_s^2 \frac{dp}{d\eta} (c_s^2 \bar{\Theta}) + \frac{1}{k^2 c_s^2} [A_u \bar{\Theta} + c_s^2 \theta_2 \Theta] = - \frac{3}{k^2} \Phi - c_s^2 \frac{dp}{d\eta} (c_s^2 \bar{\Phi}), \quad (20)$$

The photon-barion fluid has slight imperturbations corresponding to shear viscosity and heat conduction in the fluid (Weinberg 1971). These imperturbations damp acoustic oscillations. To consider these effects, we now present the equations of motion of the system in their full form, including separate continuity and Euler equations for the barions. Formally the continuity and Euler equations follow from the covariant conservation of the joint stress-energy tensor of the photon-barion fluid. Because photon and baryon numbers are separately conserved, the continuity equations are unchanged,

$$\Theta = -\frac{3}{k} \dot{\alpha}_b - \dot{\Phi}, \quad \dot{\alpha}_b = -k \dot{\alpha}_b - 3 \dot{\Phi}, \quad (18)$$

The Euler equations contain qualitatively new terms where  $\dot{\alpha}_b$  and  $\dot{\alpha}_r$  are the density perturbation and fluid velocity of the barions.

For the baryons the first term on the right accounts for cosmological expansion, which makes momenta decay as  $a^{-1}$ . The third term on the right accounts for momentum exchange in the Thomson scattering between photons and electrons (protons are very tightly coupled to electrons via Coulomb scattering), with  $\tau \equiv n_{\text{eff}} a$  the differential Thomson optical depth, and is compensated by its opposite in the photon Euler equation. These terms are the origin of heat conduction in the photon-barion fluid. The Euler equations are very simple if we neglect the difference in the Thomson scattering between photons and electrons (momentum exchange is negligible in the Thomson scattering via Coulomb scattering), with  $\tau \ll 1$  and  $n_{\text{eff}} \ll 1$  the photon Euler equation. These terms are the origin of heat conduction in the photon-barion fluid. The Euler equations are

Building 9.6

Hu & Dodelson

The small scale limit, where spherical harmonics analysis coincides with Fourier analysis (Seljak 1997). Then the wavevector  $\mathbf{k}$  picks out a preferred direction against the polarization direction in equation 45. Positive and negative  $B$ . In linear theory, scalar perturbations like the gravitational potential and temperature perturbations have only one intrinsic direction associated with them, that provided by  $\mathbf{k}$ , and the orientation of the polarization inevitably takes it from that one direction, thereby producing an  $E$ -mode. The generalization to an all-sky characterization of the polarization changes none of these qualitative features. The  $E$ -mode and the  $B$ -mode are formally distinguished by the orientation of the Hessian of the Stokes parameters which define the direction of the polarization itself. This geometric distinction is preserved under summation of all Fourier modes as well as the generalization of Fourier analysis to spherical harmonics analysis.

The acoustic peaks in the polarization spectrum appear exclusively in the EE power spectrum of Equation (5). This distinction is very useful as it allows a clean separation of this effect from those occurring beyond the scope of the linear perturbation theory of scalar fluctuations: in particular, gravitational waves (see §4.2.3) and gravitational lensing (see §4.2.4). Moreover, in the working cosmological model, the polarization peaks and correlations are precisely predictable given the source properties and their projection into multipole moments.

The discussion in the previous sections suffices for a qualitative understanding of the acoustic peaks in the power spectrum we must consider more carefully the sources of anisotropies. To refine this treatment we must take into account the effects of temperature as they appeared on a spherical shell at  $\mathbf{x} = D^* \hat{\mathbf{n}}$  in effective temperature at the present epoch, and the distance between recombination, where  $\hat{\mathbf{n}}$  is the direction vector, and  $D^* = \eta_0 - \eta_*$  is the distance from the last scattering surface to the present time. An observer today sees the acoustic oscillations at added level of complexity. An observer today sees the acoustic oscillations today has the projection of inhomogeneities at the acoustic oscillations takes place in Fourier space, because the description of the acoustic oscillations and the source properties and their projection into multipole moments.

Equation (6) in terms of spherical harmonics, so the observed anisotropy today solved for the Fourier amplitude [ $\Theta + \Psi(k, \eta_*)$ ], we can expand the expansion integral in eight can travel between recombination and the present (see Plate 3). Having recombination, where  $\hat{\mathbf{n}}$  is the direction vector, and  $D^* = \eta_0 - \eta_*$  is the distance between recombination and the present time. An observer today sees the acoustic oscillations today has the projection of inhomogeneities at the acoustic oscillations and the source properties and their projection into multipole moments.

### 3.8 Integral Approach

In linear theory, scalar perturbations like the gravitational potential and temperature fluctuations have only one intrinsic direction associated with them, that provided by  $K$ , and the orientation of the polarization inevitably takes it from that one direction, thereby producing an  $E$ -mode. The generalization to an all-sky characterization of the polarization changes none of these qualitative features. The  $E$ -mode and the Stokes parameters which define the direction of the Hessian of the  $B$ -mode are formally distinguished by the five features. The  $B$ -mode and the  $E$ -mode are formally distinguished by the orientation of the Stokes parameters which define the direction of the polarization itself. This geometric distinction is preserved under summation of all Fourier modes as well as the generalization of Fourier analysis to spherical harmonics and beyond.

The acoustic peaks in the polarization appear exclusively in the  $EE$  power spectrum of Equation (5). This distinction is very useful as it allows a clean separation of those effects from those occurring beyond the scope of the linear perturbation theory of scalar fluctuations (see §4.2.3) and gravitational lensing (see §4.2.4). Moreover, in the working cosmological model, the polarization peaks and correlations are precise predictions of the model, while the implications of the same physics. As such their detection would represent a sharp test on the implicit assumptions of the working model.

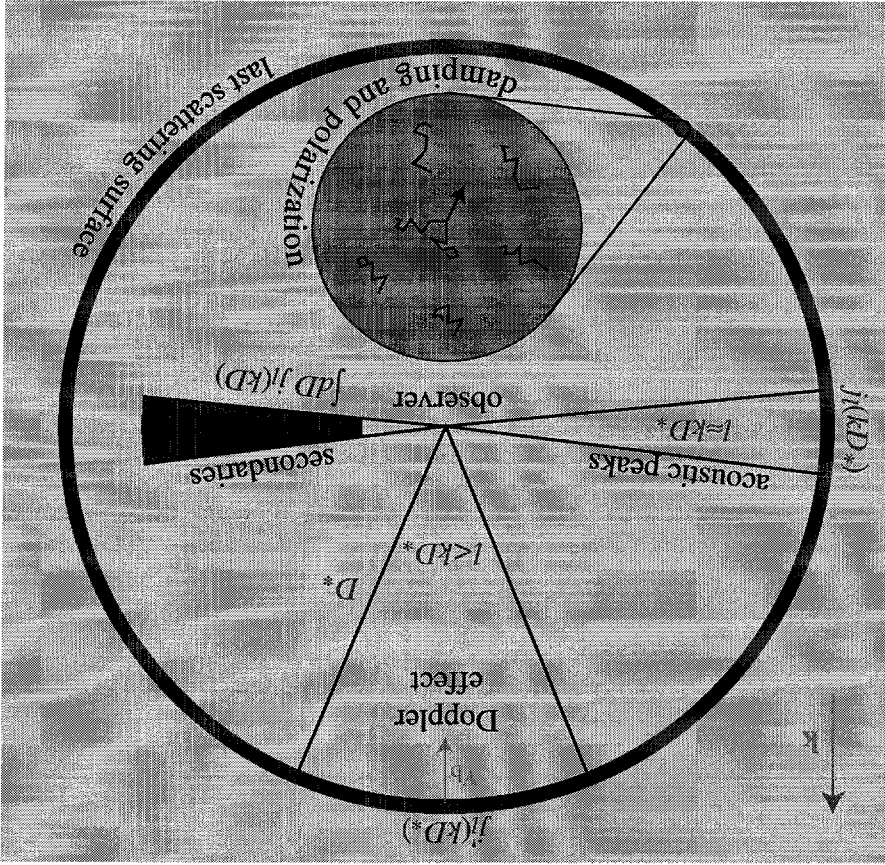
Until now, we have focused on the polarization strength without regard to its orientation. The orientation, like a 2 dimensional vector, is described by two components  $E$  and  $B$ . The  $E$  and  $B$  decomposition is simplest to visualize in

The fact that the polarization strength is of order the quadrupole explains the shape and height of the polarization spectrum in Plate I b. The monopole and dipole  $\Theta$  and  $u_y$  are of the same order of magnitude at recombination, but their oscillations are  $\pi/2$  out of phase as follows from Equation (9) and Equation (10). Since the quadrupole is of order  $k_y^2/k_x^2$  (see Figure 3), the polarization spectrum should be smaller than the temperature spectrum by a factor of order  $k_x/k_y$  at recombination. As in the case of the damping, the precise value requires numerical work (Bond & Efstathiou 1987) since  $\tau$  changes so rapidly near recombination. Calculations show a steady rise in the polarized fraction with increasing  $k$  or  $a$  to a maximum of about ten percent before damping destroys the oscillations and hence the dipole source. Since  $u_y$  is out of phase with the monopole, the polarization peaks should also be out of phase with the monopole peaks. Indeed, Plate I b shows that this is the case. Furthermore, the phase relation also tells us that the polarization is correlated with the temperature perturbations. The correlation power  $C_{EE}$  being the product of the two, exhibits oscillations at twice the acoustic frequency.

Unlike the reflection of sunlight off of a surface, the incoming radiation comes from all angles. If it were completely isotropic in intensity, radiation coming along the  $\hat{x}$  would provide the polarization state that is missing from that coming along  $\hat{y}$  leaving the net outgoing radiation unpolarized. Only a quadrupole temperature anisotropy in the radiation generates a net linear polarization from Thomson motion of photons and there only if the Universe is optically thin to Thomson scattering (i.e. it is inversely proportional to  $r$ ). Polarization generates the scattered light. As we have seen, a quadrupole can only be generated causally by the generation suffers from a Catch-22: the scattering which generates polarization scatters across this scale (i.e. it is inversely proportional to  $r$ ).

The dissipation of the acoustic oscillations leaves a signature in the polarization of CMB in its wake (see e.g. Hu & White 1997a and references therein for a more complete treatment). Much like reflection off of a surface, Thomson scattering induces a linear polarization in the scattered radiation. Consider incoming radiation in the  $-x$  direction scattered at right angles into the  $z$  direction (see Plate 2, left panel). Heuristically, incoming radiation shakes an electric field vector or polarization parallel to the outgoing polarization (see one polarization state. More generally, the Thomson differential cross section that is polarized parallel to the outgoing direction cannot scatter leaving only polarization  $\epsilon$  must be orthogonal to that direction. However since the outgoing polarization parallel to that direction, Thomson radiation is polarized along the same direction as the electric field vector.

Plate 3: Integral approach. CMB anisotropies can be thought of as the line-of-sight projection of various sources of plane wave temperature and polarization fluctuations: the acoustic effective temperature and velocity or Doppler effect (see §3.8), the quadrupole sources of polarization over which they contribute is thick compared with the last scattering surface at recombination and the typical wavelength of a perturbation.



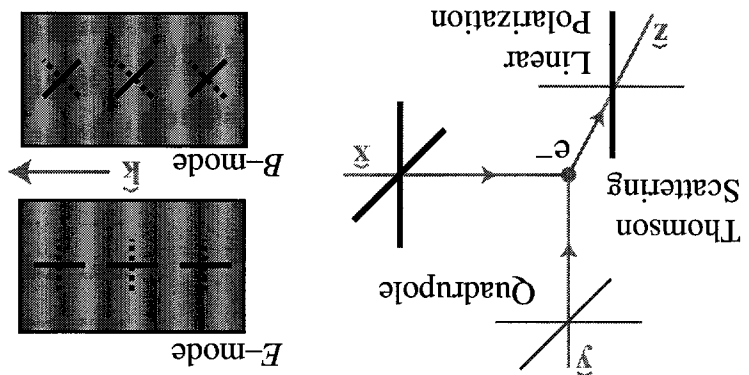
Hu & Dodelson

Projection is less straightforward for other sources of anisotropy. We have hindered to neglect the fact that the acoustic motion of the photon-rayon fluid also produces a Doppler shift in the radiation that appears to the observer as a temperature anisotropy as well. In fact, we argue above that  $u^a \approx u_1$  is of comparable magnitude but out of phase with the effective temperature. If the Doppler effect projected in the same way as the effective temperature, it would wash out the acoustic peaks. However, the Doppler effect has a directional dependence as well since it is only the line-of-sight velocity that produces the effect. Formally, it is a dipole source of temperature anisotropies and hence has an  $\ell = 1$  structure. The coupling of the dipole and plane wave angular

where the projected source  $u(k) = [\theta + \Psi](k, \eta, j)(kD)$ . Because the spherical harmonics are orthogonal, Equation (1) implies that  $\Theta_{lm}$  today is given by the integral in square brackets today. A given plane wave actually produces a range of anisotropies in angular scale as is obvious from Plate 3. The one-to-one mapping between wavenumber and multipole moment described in Fig. 3.1 is only approximate and  $k$  is one-to-one (see Plate 3).

$$\Theta(\mathfrak{a}, \eta_0) = \sum_{m=0}^{\infty} Y_m \sum_{k=0}^m a_k \int_{\mathbb{R}} (-i)^k \frac{(2\pi)^3}{d_{\mathfrak{a}}^3} \chi_{*} X_m^k(\mathfrak{a}) d\mathfrak{a} \quad (21)$$

Plate 2: Polarization generation and classification. Left: Thomson scatterings of quadrupole temperature anisotropies (depicted here in the  $x - y$  plane) generates linear polarization. Right: Plate is parallel or perpendicular to the wavevector  $\mathbf{k}$  is called the  $E$ -mode and the one at  $45^\circ$  angles is called the  $B$ -mode.



23

and  $\Delta R^*/R \approx 1.0\Delta Q_0 h^2/\phi_0 h^2$ . Current observations indicate that  $\epsilon_c = 304 \pm 4$ , and  $\epsilon_{eff} = 168 \pm 15$ ,  $\ell_d = 1392 \pm 18$ ,  $R^* = 0.60 \pm 0.06$ , and  $n = 0.96 \pm 0.04$  (Knox et al 2001; see also Wang et al 2001; Fryke et al 2001; de Bernardi et al 2001), if gravitational waves contributions are subdominant and the reionization redshift is low as assumed in the working cosmological model (see §2.1).

$$\begin{aligned} \frac{\Delta \ell_a}{\ell_a} &\approx -0.24 \frac{\Delta m^2_h}{\Delta m^2_h} + 0.07 \frac{\Delta b^2_h}{\Delta b^2_h} - 0.17 \frac{\Delta a}{\Delta a} - 1.1 \frac{\Delta u_{tot}}{\Delta u_{tot}}, \\ \frac{\Delta \ell_{eq}}{\ell_{eq}} &\approx 0.5 \frac{\Delta m^2_h}{\Delta m^2_h} - 0.17 \frac{\Delta a}{\Delta a} - 1.1 \frac{\Delta u_{tot}}{\Delta u_{tot}}, \\ \frac{\Delta \ell_d}{\ell_d} &\approx -0.21 \frac{\Delta m^2_h}{\Delta m^2_h} + 0.20 \frac{\Delta b^2_h}{\Delta b^2_h} - 0.17 \frac{\Delta a}{\Delta a} - 1.1 \frac{\Delta u_{tot}}{\Delta u_{tot}}, \end{aligned} \quad (24)$$

In the model of Plate I, these numbers are  $\ell_a = 301$  ( $\ell_1 = 0.73\ell_a$ ),  $\ell_{eq} = 149$ ,  $\ell_d = 1332$ ,  $R_s = 0.57$  and  $n = 1$  and in this family of models the parameter sensitivity is approximately (Hu et al 2001)  $\text{spectrum.}$

The phenomenology of the acoustic peaks in the temperature and polarization is essentially described by 4 observables and the initial conditions (Hu et al 1997). These are the angular extrema of the sound horizon  $\zeta \equiv nD/s$ , the particle horizon  $\zeta_0$  at matter radiation equality  $\zeta_0 \equiv k_0 D^*$ , and the damping scale  $\zeta_d \equiv k_0 D^*$ . As well as the value of the baryon-photon momentum density ratio  $R$ ,  $\zeta_d$  sets the spacing between of the peaks;  $\zeta_d$  and  $D$  compete to determine their amplitude and odd peaks. The initial conditions set by  $\zeta_0$ , fixes the modulation of the even and odd peaks in units of  $\zeta$ , and an overall tilt  $n$  in the power spectrum.

### 3.9 Parameter Sensitivity

of the observables is then limited only by the precision in the prediction of the non-linear physics even though the CMB responds linearly as we shall see in §4. Perhaps more importantly, the widely-used CAMB<sup>4</sup> code (Seljak & Zaldarriaga 1996) explores these properties to calculate the anisotropies in linear perturbation theory. It numerically solves for the smooth-varying sources on a sparse grid in wavenumber, interpolating in the integrals for a handful of its smooth variables. It has largely replaced the original ground-breaking codes (Wilson & Silk 1981; Bond & Efstathiou 1984; Vittorio & Silk 1984) based on tracking the rapid temporal oscillations of the multipole moments that simply reflect structure in the spherical Bessel functions themselves.

This formulation of the anisotropies in terms of projections of sources with specific local angular structure can be completed to include all types of sources of temperature and polarization anisotropies at any given epoch in time linear or non-linear: the monopole, dipole and quadrupole sources arising from perturbations, vorticity and gravitational waves (Hu & White 1997b). In a curved geometry one replaces the spherical Bessel functions with ultraspherical Bessel functions (Abbott & Schaefer 1986; Hu *et al* 1998). Precision in the predictions

$$C_i = \frac{2}{\pi} \int dk k^3 a_i^*(k). \quad (23)$$

The last term vanishes for constant gravitational potentials, but is non-zero if residual radiation driving exists, as it will in low  $Qm^2$  models. Note that residual radiation driving is particularly important because it adds in phase with the monopole: the potentials vary in time only near recombination, so the Bessel function can be set to  $j_1(kD)$  and removed from the integral. This combination has the effect of decreasing the multipole value of the first peak  $\ell_1$ , as the matter-radiation ratio at recombination decreases (Hu & Sugiyama 1995). Finally, we mention that the varying potentials also play a role at very late times due to non-linearities or the importance of a cosmological constant for example. Those contributions, to be discussed more in §4.2.1, are sometimes referred to as late integrated Sachs-Wolfe effects, and do not add coherence with  $[0 + \Psi](\eta^*)$ .

$$+ (*D\Phi)^\mu_\nu (*u^\nu \Phi)^\alpha + (*D\Phi)^\mu_\nu (*u^\nu \Theta)^\alpha = (\Phi \circ u)^{\mu}_\nu (\Phi + \Theta)^\alpha. \quad (22)$$

There is one more subtley involved when passing from acoustic oscillations to antisolitopes. Recall from §8.5 that radiation leads to decay of the gravitational potentials. Residual radiation after decoupling therefore implies that the effective temperature is not precisely  $(\Theta + \frac{1}{4}\eta)$ . The photons actually have slightly shallower potentials to climb out of and lose the perturbative analogue of the cosmological redshift, so the  $(\Theta + \frac{1}{4}\eta)$  overestimates the difference between the true photon temperature and the observed temperature. This effect of course is already in the continuity equation for the monopole Equation (18) and so the source in Equation (21) gets generalized

momenta imply that in the projection of the Doppler effect involves a combination of  $j_1 \mp 1$  that may be rewritten as  $j_1(x) \equiv dj_1(x)/dx$ . The structure of  $j_1$  lacks a strong peak at  $x = 0$ . Physically this corresponds to the fact that the velocity is irrotational and hence has no component in the direction orthogonal to the wavevector (see Plate 3). Correspondingly, the Doppler effect cannot produce strong peaks structures (Hu & Sugiyama 1995). The observed peaks must be wavevector (see Plate 3).

tributions, and even the existence of primordial gravity waves, so the potential intervening dark matter, dark energy, baryonic gas density and temperature disrupt secondary temperature and polarization anisotropies. These depend on the temperature of the Universe at their journey from the recombination epoch, they pick up a wealth of information about the evolution of structure in the Universe and its origin in the early Universe. As CMB photons traverse the large scale structures of the Universe, they scatter the peaks of microwave background radiation. Beyond and beneath the peaks lies a wealth of information about the evolution of structure in the Universe, and eventually the days of splendid isolation of cosmic microwave background radiation have been scaled, the days of acoustic peaks in the temperature and polarization power spectra have

## 4 BEYOND THE PEAKS

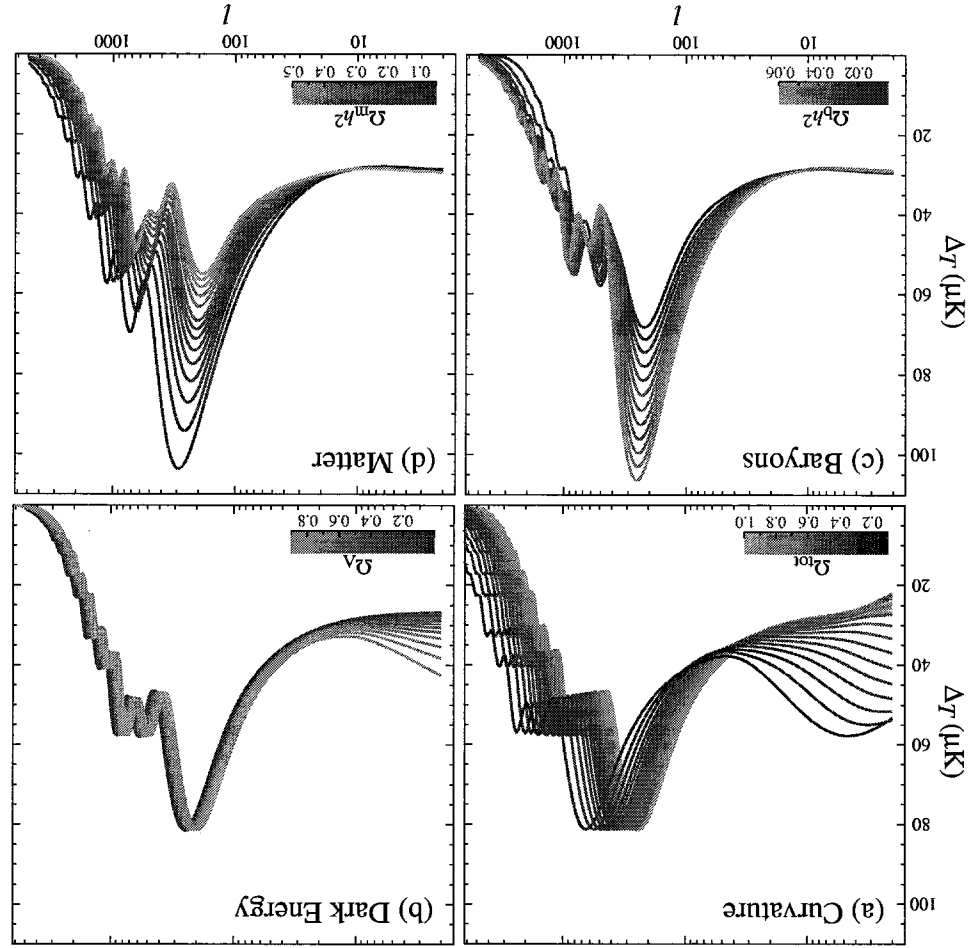
The upshot is that precise measurements of the acoustic peaks yield precise determinations of four fundamental parameters of the working cosmological model:  $\Omega_m h^2$ ,  $\Omega_b h^2$ ,  $D_s$ , and  $n$ . More generally, the first three can be replaced by  $\ell_{\text{eff}}$ ,  $\Omega_m h^2$ ,  $\Omega_b h^2$ ,  $D_s$ , and  $n$ . To extend these results to models where the underlying assumptions of the working model are violated, it implies  $\Omega_m < 1$  but at low significance currently.

Relatively low  $\Omega_m h^2$  that is preferred in the CMB data, it implies  $\Omega_m < 1$  but at the measurements of a relatively high Hubble constant  $h \approx 0.7$ ; combined with a direct evidence for  $\Omega_m < 1$  from local structures in the Universe. The second is lowing for external information. The most important is the nearly overreaching effects. The evidence for dark energy through the CMB comes about by allowing for external information. This is called the angular diameter distance to measure the peaks alone since it only takes a small amount of curvature to isolate the effects. The down side is that dark energy can never be isolated through values of  $\Omega_A$ . The down side is that dark energy can never be isolated reasonably so small, it only creates a correspondence small ambiguity in  $\Omega_m$  for transically beyond the cosmological constant assumed here. Since the effect of  $\Omega_A$  is in-eracy in the literature and can readily be generalized to dark energy components they both appear only in  $D_s$ . This is called the angular diameter distance degeneracy.

There remains a weak but perfect degeneracy between  $\Omega_m$  and  $\Omega_A$  because they both contain a built-in consistency check. What makes the peaks so valuable for this test is that the rules are standardize-e.g., recombination and the energy contents of the Universe during this epoch, additional consistency check on the implicit assumptions in the working model, measurement of the baryon-photon ratio  $R_s$ . The damping scale  $\ell_d$  provides an degeneracy of  $\Omega_m$  on the barions can likewise be broken from a popular belief, any one of these alone is not a standard ruler whose absolute scale is known even in the working cosmological model. This is reflected in the combination with a measurement of the matter-radiation ratio from  $\ell_{\text{eff}}$ , this dependence of  $\ell_d$  on  $\Omega_m h^2$  and hence the Hubble constant is quite strong. But sensitivity of these scales to other cosmological parameters. For example, the dependence of  $\ell_d$  on  $\Omega_m h^2$  and hence the Hubble constant is quite strong. But dependence of  $\ell_d$  on the other cosmological parameters. This is reflected in the scale is broken.

The weaker degeneracy of  $\Omega_m$  on the barions can likewise be broken from a popular belief, any one of these alone is not a standard ruler whose absolute scale is known even in the working cosmological model. This is reflected in the combination with a measurement of the matter-radiation ratio from  $\ell_{\text{eff}}$ , this dependence of  $\ell_d$  on  $\Omega_m h^2$  and hence the Hubble constant is quite strong. But dependence of  $\ell_d$  on the other cosmological parameters. This is reflected in the scale is broken.

Plate 4: Sensitivity of the acoustic temperature spectrum to four fundamental cosmological parameters (a) the dark energy as quantified by  $\Omega_m$ , (b) the dark energy as quantified by  $\Omega_A$ , (c) the physical baryon density  $\Omega_b h^2$ , (d) the physical matter density  $\Omega_m h^2$ , all varied around a fiducial model of  $\Omega_m = 1$ ,  $\Omega_b = 0.65$ ,  $\Omega_b h^2 = 0.02$ ,  $\Omega_m h^2 = 0.147$ ,  $n = 1$ ,  $z_m = 0$ ,  $E_s = 0$ .



In particular, since this non-linear scale also corresponds to galaxy clusters across a wide range of scales.

4.1.2 COSMOLOGICAL IMPPLICATIONS The combination of the COBE normalisation and the matter transfer function and the near scale-invariant initial spectrum of fluctuations tells us that by the present fluctuations in the cold dark matter or baryon density fields will have gone non-linear for all scales  $k \gtrsim 10^{-1} h\text{Mpc}^{-1}$ . It is a great triumph of the standard cosmological paradigm that there is just enough growth between  $z^2 \approx 10^3$  and  $z = 0$  to explain structures in the Universe.

On scales below the horizon at matter-radiation equality, we have seen in §3.5 that pressure gradients from the acoustic oscillations themselves impede the clustering of the dominant component, i.e. the photons, and lead to decay in the potential. Dark matter density perturbations remain but grow only logarithmically from the value at horizon crossing, which (just as for large scales) is approximately the initial potential,  $\delta_m \approx -\Psi$ . The potential for modes that have entered the horizon already will therefore be suppressed by  $\Psi \propto -6m/k^2 \sim \Psi_0/k^2$ , while it falls off as  $k^{-2}$  on small scales. If the barions fraction  $p_b/p_m$  is sub-stellar, baryons alter the transfer function in two ways. First their inability to cluster below the sound horizon causes further decay in the potential between clusters (see Bunn & White 1997). The ratio of  $\Psi$  at late times to its initial value is called the Poisson equation. The ratio of  $\Psi$  at late times to its initial value is close to one, transfer function. On large scales, then, the transfer function is called the stationary solution in the barion field. Second the acoustic wiggles in the matter power spectrum are related to the acoustic peaks in the CMB spectrum like twins separated at birth and are actively being pursued by the largest galaxy surveys (Perivolaris et al 2001). For fitting formulae for the transfer function that include these effects see Eisenstein & Hu (1998).

$$\frac{1}{\Delta T^2} \approx \frac{g}{T^2} \approx \frac{1}{L} g_H^2, \quad (25)$$

Hu & Dodds

imately 4/3,

where the second equality follows from the Fokker-Planck equation in a fully matter-dominated universe with  $\Omega_m = 1$ . The observed CMB fluctuation of  $\Delta_T \approx 28\mu K$  (Smoot et al 1992) implies  $\delta_H \approx 2 \times 10^{-5}$ . For corrections for  $\Omega_m < 1$  where the potential decays because the dominant driver of the expansion cannot cluster,

Hu & Dodelson imately  $\Psi/3$ ,

#### 4.1 Matter Power Spectrum

4.1.1 PHYSICAL DESCRIPTION After reconstructing the pressure of the photons, the barions simply fall into the Newtonian potential wells with the cold dark matter, an event usually referred to as the end of the Compton drag epoch. We claimed in §3.5 that above the horizon at matter-radiation equality the potentials are nearly constant. This follows from the dynamics: where pressure gradients are negligible, initial matter-radiation equality causes a potential flow of  $a_{tot} \sim (k\eta)^{\frac{1}{n+1}}$ , [see Equation (19)] and causes density enhancements by continuity of  $\delta_{tot} \sim (k\eta)^{\frac{n}{n+1}}$ . The Poisson equation says that the potential at this later time  $\Psi \sim -(k\eta)^{-\frac{n}{n+1}} \sim -\Psi_0$ , so that this rate of growth is exactly right to keep the potential constant. Formally, this Newtonian argument only applies in general relativity for a particular choice of coordinates (Bardeen 1980), but the rule of thumb is that if what is driving the expansion (including spatial curvature) can also cluster unimpeded by pressure, the gravitational potential will remain constant.

The same balance between pressure and gravity that is responsible for acoustic oscillations determines the power spectrum of fluctuations in the non-relativistic matter. This relationship is often obscured by focusing on the density fluctuations in the pressurless cold dark matter itself and we so we will instead consider the matter power spectrum from the perspective of the Newtonian potential.

We begin in §4.1 with a discussion of the matter power spectrum to set the framework for the discussion of secondary anisotropies. Secondaries can be divided into two classes: those due to gravitational tidal effects and those induced by scattering off of electrons. The former are treated in §4.2 and the latter in §4.3. Secondary anisotropies are often non-Gaussian, so they show up not only in the power spectra of §2, but in higher point functions as well. We briefly discuss non-Gaussian statistics in §4.4. All of these topics are subtopics of current research to which this review can only serve as introduction.

The payoff of their detection is enormous. The price for this extended reach is the loss of the ability both to make precise predictions, due to uncertainty and/or nonlinearities, and to make precise measurements, due to the cosmic variance of the primary properties and the relative lack of importance of galactic and

The ISW effect thus generically shows up only at the lowest  $\ell$ 's in the power spectrum (Kofman & Starobinsky 1985). This spectrum is shown in Plate 5. Secondary anisotropy predictions in this figure are for a model with  $Q_{\text{tot}} = 1$ ,  $Q_A = 2/3$ ,  $Q_B^2 = 0.02$ ,  $Q_m^2 = 0.16$ ,  $n = 1$ ,  $z_n = 7$  and inflationary energy scale  $E_c \ll 10^{16}$  GeV. The ISW effect is especially important in that it is extremely sensitive to the dark energy: its amount, equation of state and clustering properties (Coble et al 1997; Caldwell et al 1998; Hu 1998). Unfortunately, being conformed to the low multipoles, the ISW effect suffers severely from the cosmic variance in Equation (4) in its detectability. Perhaps more promising is its correlation with other observations.

The ISW projection, indeed the projection of all secondaries, is much different (see Plate 3). Since the duration of the potential change is much longer, photons typically travel through many peaks and troughs of the perturbation. This camouflages the effect of the modes which do have an impact on the photon temperature. The only modes which do have an impact are those with wavevectors perpendicular to the line of sight, so that along the line of sight the photon does not pass through crests and troughs. What fraction of the modes contribute to the effect then? For a given wavenumber  $k$  and line of sight instead of the full spherical shell at radius  $4\pi k^2 dk$ , only the ring  $2\pi dk$  with  $k \leq l$  participate. Thus, the anisotropy induced is suppressed by a factor of  $k$  (or  $\ell$ ) in angular space. Mathematically, this arises in the time-of-flight integral of Equation (23) from the integral over the oscillatory Bessel function  $\int dx j_\nu(x) \approx (\pi/2e)^{1/2}$  (see Plate 3).

Potential decay due to residual radiation was introduced in §3.8, but that due to dark energy or curvature makes the dark energy much different changes in the anisotropy spectrum. What makes the dark energy or curvature contributions different from those due to radiation is the longer length of time over which the potentials decay, on order the Hubble time today. Residual radiation produces its effect quickly, so the distance over which photons feel the effect is much smaller than the wavelength of the potential fluctuation. Recall that this means that in the integral in Equation (23) could be set to  $j_1(kD^*)$  and removed from the integral. The final effect then is proportional to  $j_1(kD)$ , and adds in phase.

4.2.1 ISW EFFECT As we have seen in the previous section, the potential barrier  $\Omega_m < 1$  model at the end of matter domination and the onset dark energy (or spatial curvature) domination. If the potential decays between the time a photon falls into a potential well and when it climbs out it gets a boost in temperature of  $\delta\Phi$  due to the differential gravitational redshift and  $-\delta\Phi \approx 6\%$  due to an accompanying contraction of the wavelength (see §3.3).

### Polarization.

Gravitational secondaries arise from two sources: the different redshift from time-variable metric perturbations (Sachs & Wolfe 1967) and gravitational lensing. There are many examples of the former, one of which we have already encountered in §3.8 in the context of potential decay in the radiation dominated era. Such gravitational effects are usually called the integrated Sachs-Wolfe (ISW) effect in linear perturbation theory (§4.2.1), the Rees-Sclama (§4.2.2) effect in the non-linear regime, and the gravitational wave tensor perturbations (§4.2.3). Gravitational waves and lensing also produce  $B$ -modes in the polarization (see §3.7) by which they may be distinguished from acoustic

## 4.2 Gravitational Secondaries

The combination is even more fruitful in the relationship between the acoustic peaks and the barion wiggles in the matter power spectrum. Our knowledge of the physical distance between adjacent wiggles provides the ultimate standard candle for cosmology (Eisenstein et al 1998). For example, at very low  $z$ , the radial distance of the true physical distance corresponds to a  $Mpc$ , and a knowledge of the true physical distance determines the matter power spectrum out to a galaxy is  $c z / H_0$ . The unit of distance is therefore  $h^{-1}$   $Mpc$ , and a knowledge of the true physical distance corresponds to a  $Mpc$ . At higher redshifts, the radial distance depends sensitively on the background cosmology (especially the dark energy), so a future measurement of baryonic wiggles at  $z \sim 1$  say would be a powerful test of dark energy models. To a lesser extent, the shape of the transfer function, which mainly depends on the matter-radiation scale in  $h Mpc^{-1}$ , i.e.  $\Omega_m h$ , is another standard ruler (see e.g., Tegmark et al 2001 for a recent assessment), more heralded than the wiggles, but less robust due to degeneracy with other cosmological parameters.

For scales corresponding to  $k \gtrsim 10^{-1} h Mpc^{-1}$ , density fluctuations are non-linear and the properties of the barionic gas. We shall see that both enter into certain halo halos have been extensively studied in the working cosmological model. Less for a review). The statistical properties of the dark matter and the dark matter is bound up in a hierarchy of virialized structures or halos (see Bereschinger 1998 is the present. Numerical  $N$ -body simulations show that the dark matter linear by the present. Numerical  $N$ -body simulations are now -

the consideration of secondary CMB anisotropies.

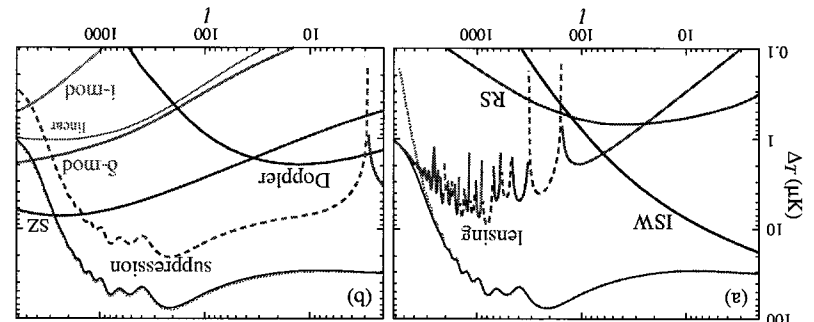
and is one of the strongest pieces of evidence for the parameters in the working cosmological model (Ostriker & Steinhardt 1995; Krauss & Turner 1995). More generally, the comparison between large-scale structure and the CMB is important in that it breaks degeneracies between effects due to deviations from power law initial conditions and the dynamics of the matter and energy contents of the Universe. Any dynamical effect that reduces the amplitude of the matter power spectrum corresponds to a decay in the Newtonian potential that boosts the level of anisotropy (see §3.5 and §4.1). Massive neutrinos are a good example of physics that drives the matter power spectrum down and the CMB spectrum

Figure 4: Gravitational waves and the energy scale of inflation  $E_i$ . Left: Temperature and polarization spectra from initial scale invariant gravitational wave spectrum with power  $\propto E_i^n$  ( $n = 4 \times 10^{16}$  GeV $^4$ ). Right: 95% confidence upper limits statistical significance achieved on  $E_i$ ; and the scalar tilt  $n$  by the MAP and Planck satellites as well as an ideal experiment out to  $\ell = 3000$  in the presence of gravitational lensing  $B$ -modes.

4.2.2 REES-SCAMMA AND MOVING HALO EFFECTS The ISW effect is linear in the perturbations. Canonicalization of the ISW effect on small scales leaves second order and non-linear analogues in its wake (Rees & Scrima 1998). From a single isolated structure, the potential along the line of sight can change not only from evolution in the density profile but more importantly from bulk motion across the line of sight. In the context of clusters of galaxies, this is called the moving cluster effect (Birkinshaw & Gull 1983). More generally, the bulk motion of dark matter halos of all masses contribute to this effect (Tulane & Laguna 1995; Sefajak 1996b), and their clustering gives rise to a low level of anisotropies on a range of scales but is never the leading source of secondary anisotropies on any scale (see Plate 5a).

4.2.3 GRAVITATIONAL WAVES A time-variable tensor metric perturbation similarly leaves an imprint in the temperature anisotropy (Sachs & Wolfe 1967). A tensor metric perturbation can be viewed as a standing gravitational wave and produces a quadrupolar distortion in the spatial metric. If its amplitude changes, it leaves a quadrupolar distortion in the CMB temperature distribution (Polarer

Plate 3: Secondary anisotropies. (a) Gravitational secondaries:  $ISW$ , lensing and Red-*Shees*-Sictama moving halo effects. (b) Scattering secondaries: Doppler, density (g) and ionization (i) modulated Doppler, and the SZ effects. Curves and model are described in the text.



relaxation with other tracers of the gravitational potential (e.g., X-ray background Boughez et al. 1998 and gravitational lensing, see §4.2.4).

**4.3.1. PEAK SUPERPOSITION** Like scattering below the recombination, scattering at late times suppresses antiisotropies in the distribution that have already formed. Recombination therefore suppresses the amplitude of the acoustic peaks by the fraction of photons scattered, approximately the optical depth  $\sim T_1^4$  (see Plate 5b), dotted line and negative, dashed line, contribution corresponding to  $|\delta\Delta_{T_1}^{(1)}|$ . Between the  $z_m = \tau$  and  $z_m = 0$  models, unlike the plasma before recombination, the medium is optically thin and so the mean free path and diffusion length of the photons is of order the horizon itself. New acoustic oscillations cannot form. On scales approaching the horizon at reionization, inhomogeneities have yet to be converted into anisotropies (see § 3.8) and so large-angle fluctuations are not suppressed. While these effects are relatively large compared with the expected precision of future experiments, they might change in the overall normalization of fluctuations except at the lowest, cosmic variance limited, multipoles.

from the observations both of the lack of a Gunn-Peterson trough (Gunn & Peterson 1965) in quasar spectra and its prehmimary detection (Becker et al 2001), we know that hydrogen was ionized at  $z \gtrsim 6$ . This is thought to occur through the ionizing radiation of the first generation of massive stars (see e.g. Loeb & Barkana 2001 for a review). The consequent recoupling of CMB photons to the barions causes a few percent of them to be re-scattered. Interestingly, three changes to the photon distribution: suppression of primordial anisotropy, generation of large angle polarization, and a large Doppler effect. The latter two are suppressed on small scales by the cancellation of effects. The latter two are suppressed on small scales by the cancellation of effects.

### 4.3 Scattering Secondaries

Because the lensed CMB distribution is not linear in the fluctuations, it is not completely described by changes in the power spectrum. Much of the recent work in the literature has been devoted to utilizing the non-Gaussianity to isolate lensing effects (Bernardeau 1997, 1998; Zaldarriaga & Seljak 1999; Zaldarriaga 2000) and their cross-correlation with the ISW effect (Goldberg & Spergel 1999; Seljak & Zaldarriaga 1999). In particular, there is a quadratic combination of the anisotropy data that optimally reconstructs the projected dark matter potentials from use in this cross-correlation (Hu 2001c). The cross correlation is especially important in that it is a flat universe, it is a direct indication of dark energy and can be used to study the properties of the dark energy beyond a simple equation of state (Hu 2001b).

Hu & Dodson

Gravitational lensing also generates a small amount of power in the anisotropies of sky (Hu 2001b). Inhomogeneous distribution of lenses introduces ripples in the gradient on the antisotropy of the CMB as approximatively a pure gradient on the sky and the destroyed the primary anisotropies (see Plate 5). On these small scales, the lensing also generates a small amount of power in the anisotropies of sky (Hu 2001b).

This large coherence and small amplitude ensures that linear theory in the one-to-one mapping of the source and image planes is simply distorted the images formed from the source and image oscillations in accord with the deflection angle. This warping naturally also distorts the mapping of physical scales in the acoustic peaks to angular scales §8 and hence smooths features in the temperature and polarization (Seljak 1996a). The smoothing scale is the coherence scale of the deflection angle  $\Delta\zeta \approx 60$  and is sufficiently wide to alter the acoustic peaks with  $\Delta\zeta \sim 300$ . The contributions, shown in Plate 5a are therefore negative (dashed)

**4.2.4 GRAVITATIONAL LENSING** The gravitational potentials of large-scale structure also lens the CMB photons. Since lensing conserves surface brightness, it only affects anisotropies and hence is second order in perturbation theory (Blanchard & Schmidler 1987). The photons are deflected according to the angular gradient of the potential projected along the line of sight with a weighting of  $2(D^* - D)/(D^* + D)$ . Again the cancellation of parallel modes implies that it is mainly the large-scale potentials that are responsible for deflections. Specifically, the angular gradient of the potential peaks at a multipole  $\ell \sim 60$  compared to scales of a  $k \sim$  few  $10^{-2} \text{ Mpc}^{-1}$  (Hu 2000b). The deflections are therefore coherent below the degree scale. The coherence of the deflection should not be confused with its rms value which in the model of Plate I has a value of

a wavelength of the fluctuation (Kamionkowski et al 1997; Zaldarriaga & Seljak 1997). The  $B$ -component presents a promising means of measuring the gravitational waves from inflation and hence the energy scale of inflation (see Figure 4, right panel). Models of inflation correspond to points in the  $n, F$  plane (Dodelson et al 1997). Therefore, the anticipated constraints will discriminate among different models of inflation, probing fundamental physics at scales well beyond those accessible in accelerators.

Hu & Dodge

8

18

**LUMINAR MODULATION:** At the opposite extreme, linear density fluctuations modulate the more general density modulation.

organization MODULATION: Finally, optical depth modulation can also come from perturbations in the ionization fraction (Aghanim et al 1996; Grunzweig & Hu 1998; Knox et al 1998). Predictions for this effect are the most uncertain as it involves both the formalism of the first ionizing objects and the subsequent radiative transfer of the ionizing radiation (Briscoch et al 2000; Benson et al 2001). It however unlikely to dominate the density modulated effect except perhaps at very high multipoles ( $\ell \sim 10^4$ ) (crudely estimated, following Grunzweig & Hu 1998, a probe of the gas distribution to the gas distribution (Gorlitzky 2001).

3.5 SUNYAEV-ZEL'DOVICH EFFECT Internal motion of the gas in dark matter halos also give rise to Doppler shifts in the CMB photons. As in the linear Doppler effect, shifts that are first order in the velocity are canceled as photons scatter off of electrons moving in different directions. At second order in the velocity, there is a residual effect. For clusters of galaxies where the temperature of the gas can reach  $T \sim 10$ keV, the thermal motions are a substantial fraction of the speed of light  $v_{rms} = (3T/m_e)^{1/2} \sim 0.2$ . The second order expression involves a spectral distortion in the CMB where photons on the cooler CMB side are transferred to the Wien tail. This effect is called the thermal Sunyaev-Zel'dovich (SZ) effect (Sunyaev & Zel'dovich 1972). Because the net effect is finite, once imprinted, distortions relative to the redshifted background term effects, once imprinted, distortions relative to the gas distribution (Gorlitzky 2001).

0001; Lewis et al 2000) but gas pressure will tend to smooth out the distribution of the cores of halos and reduce small scale fluctuations. In the absence of substantial cooling and star formation, these net effects can be modeled under the assumption of hydrostatic equilibrium (Komatsu & Seljak 2001) in the halos and included in a halo approach to the gas distribution (Cooray 2001).

**GENERAL DENSITY MODULATIONS:** Both the cluster and linear modulations are dominated by the low density fluctuations. For the low reionization redshifts currently expected ( $z \approx 6 - 7$ ) most of the effect comes neither from cluster redshifts nor the linear regime but intermediate scale dark matter halos. An upper limit to the total effect can be obtained by assuming the gas traces the dark matter (Hu 2000a) and implies signs on the order of  $\Delta_T \sim \ln k / k_c < 10^3$  (see Plate 5b). Based on simulations, this assumption should hold in the outer profiles of halos (Pearce et al.

3.5 SUNYAEV-ZEL'DOVICH EFFECT Internal motion of the gas in dark matter halos also give rise to Doppler shifts in the CMB photons. As in the linear Doppler effect, shifts that are first order in the velocity are canceled as photons scatter off of electrons moving in different directions. At second order in the velocity, there is a residual effect. For clusters of galaxies where the temperature reaches  $T \sim 10\text{keV}$ , the thermal motions are a substantial fraction of the speed of light  $v_{rms} = (3T/m_e)^{1/2} \sim 0.2$ . The second order effect represents net transfer of energy between the hot electron gas and the cooler CMB and leaves a spectral distortion in the CMB where photons on the Rayleigh-Jeans side are transferred to the Wien tail. This effect is called the thermal Sunyaev-Zel'dovich (SZ) effect (Sunyaev & Zeldovich 1972). Because the net effect is of order  $T_{\text{cluster}} T_e / m_e \propto n_e T_e$ , it is a probe of the gas pressure. Like all CMB effects, once unperturbed, distortions relative to the redshifted background temperature remain unaffected by cosmological dimming, so one might hope to find

**CLOUDER MODULATIION:** The strongly non-linear modulation provided by the presence of a galaxy cluster and its associated gas leads to the kinetic Sunyaev-Zel'dovich effect. Clusters optical depths on order  $10^{-2}$  and peculiar velocities of  $10-3$  imply significant gas at individual scale clusters of  $10-5$  regime in the  $10-5$  range which are of course rare objects. While this signal is reasonably large, it is generally dwarfed by the thermal Sunyaev-Zel'dovich effect (see § 4.3.5) and has yet to be detected with high significance (see Claesstrom et al 2001 and references therein). The kinetic Sunyaev-Zel'dovich effect has negligible impact on the power spectrum of anisotropies due to the rarity of clusters and can be included as part

ON MODULATION: Finally, optical depth modulation can also come from variations in the ionization fraction ( $A_{\text{H}\alpha}$ ) and density ( $\rho$ ). The effect of density on the ionization fraction is relatively small, as the ionization fraction is primarily determined by the ionizing photon flux. The effect of density on the ionization fraction is relatively small, as the ionization fraction is primarily determined by the ionizing photon flux. The effect of density on the ionization fraction is relatively small, as the ionization fraction is primarily determined by the ionizing photon flux.

**GENERAL DENSITY MODULATIONS:** Both the cluster and linear modulations are dominant cases of the more general effect of density modulation by the large scale structure of the Universe. For the low redshifts currently expected  $z_{\text{in}} \approx 6 - 7$ , most of the effect comes neither from linear clusters nor the linear regime  $z_{\text{in}} \approx 6 - 7$  but intermediate scale dark matter halos. An upper limit to the total effect can be obtained by assuming the gas traces the dark matter (Hu 2000a) and compares signs on the order of  $\Delta_T \sim \text{few } \sqrt{k}$  at  $\ell > 10^3$  (see Plate 5b). Based on simulations, this assumption should hold in the outer profiles of halos (Pearce et al 2001, Lewis et al 2000) but gas pressure will tend to smooth out the distribution of the cores of halos and reduce small scale contributions. In the absence of substantial cooling and star formation, these net effects can be modeled under the assumption of hydrostatic equilibrium (Komatsu & Seljak 2001) in the halos and included in a halo approach to the gas distribution (Cooray 2001).

3.5 SUNAYAEV-ZEL'DOVICH EFFECT Internal motion of the gas in dark matter halos also give rise to Doppler shifts in the CMB photons. As in the linear Doppler effect, shifts that are first order in the velocity are canceled as photons scatter off of electrons moving in different directions. At second order in the velocity, there is a residual effect. For clusters of galaxies where the temperature of the gas can reach  $T_g \sim 10$  keV, the thermal motions are a substantial fraction of the gas temperature  $T_g$ , once primed, relative to the redshifting background temperature effects, once primed, distortions relative to the gas pressure. Like all CMB effects (SZ effect Sunyaev & Zel'dovich 1972). Because the net effect is of order  $T_{\text{cluster}} T_g / m_e \propto n_e T_g$ , it is a probe of the gas pressure. Like all CMB effects (SZ effect Sunyaev & Zel'dovich 1972). Because the net effect is of order  $T_{\text{cluster}} T_g / m_e \propto n_e T_g$ , it is a probe of the gas pressure.

4.3.3 DOPPLER EFFECT Nativey, velocity fields of order  $v \sim 10^{-3}$  (see e.g. Strauss & Willink 1995 for a review) and optical depths of a few percent would imply a Doppler effect that rivals the acoustic peaks themselves. That this is not the case is the joint consequence of the cancellation described in §4.2.1 and the fact that the acoustic peaks are not "Doppler peaks" (see §3.8). Since the Doppler effect comes from the peculiar velocity along the line of sight, it remains no contributions from linear modes with wavevectors perpendicular to the line of sight. But as we have seen, these are the only modes that survive cancellation (see Plate 3 and Kaiser 1984). Consequently, the Doppler effect from reionization is strongly suppressed and is entirely negligible below  $\sim 10^2$  unless the optical depth in the reionization epoch approaches unity (see Plate 5b).

ON MODULATION: Finally, optical depth modulation can also come from variations in the ionization fraction ( $A_{\text{H}\alpha}$ ) and density ( $\rho$ ). The effect of density on the ionization fraction is relatively small, as the ionization fraction is primarily determined by the ionizing photon flux. The effect of density on the ionization fraction is relatively small, as the ionization fraction is primarily determined by the ionizing photon flux. The effect of density on the ionization fraction is relatively small, as the ionization fraction is primarily determined by the ionizing photon flux.

4.3.2. LARGER-ANGLE POLARIZATION The scattered radiation becomes polarized since, as discussed in §3.8, temperature inhomogeneities, become anisotropic by projection, passing through quadrupole anisotropies when the perturbations are on the horizon scale at any given time. The result is a bump in the power spectrum of the  $E$ -polarization on angular scales corresponding to the horizon and the finite range of scales that contribute to the quadrupole, the polarization at resolution (see Plate 1). Because of the low optical depth of reionization and foreground free world, this is not beyond the reach of experiments and can be used to isolate the reionization epoch (Hogan et al 1982; Zaldarriaga et al 1997). As in the ISW effect, cancellation of contributions along the line of sight guarantees a sharp suppression of contributions along the line of sight in most directions of the unit sphere.

As we have seen, most of the secondary anisotropies are not linear and hence produce non-Gaussian signatures. Non-Gaussianity in the lensing and SZ signals will be important for their isolation. The same is true for contaminants such as galactic foregrounds. Finally the lack of an initial non-Gaussianity in the fluctuations is a testable prediction of the simplest inflationary models (Guth & Pi 1985; Bardeen et al 1983). Consequently, non-Gaussianity models (Guth & Pi 1985; Bardeen et al 1983) can be tested by choosing the distribution of non-Gaussianity in the CMB is currently a very active field of research. The primary challenge in the CMB is currently a very active field of research. The primary challenge in studies of non-Gaussianity is in choosing the statistic that quantifies it. Non-Gaussianity says what the statistic against the Gaussian "noise" of the primary challenge is to optimize the statistic that quantifies the Gaussian "noise" of the primary challenge is to address this question is not, not what it is. The secondary anisotropies and instruments or astrophysical systematics.

Early theoretical work on the bispectrum, the harmonic analogue of the three point function addressed its detectability in the presence of the cosmic variance of the Gaussian fluctuations (Luo 1994) and showed that the inflationary contribution is not expected to be detectable in most models (Allen et al 1987; Fabbri et al 1993). The bispectrum is defined by a triplet of multipoles, or configuration, that defines a triangle in harmonic space. The large cosmic variance in a given realization was suppressed by triplets of significant signals in specific bispectrum configurations that turn out to be detectable with experiments that have both high resolution and angular dynamical range but require the measurement of a wide range of configurations of the bispectrum. Data analysis challenges for measuring the bispectrum are specified by a quantum theory of multipoles that correspond to the sides and diagonals of a quadrilateral in harmonic space (Hu 2001a). The trispectrum is important in that it quantifies the covariance of the power spectrum across multiple scales that is often very strong in non-linear effects, e.g. the SZ effect (Crocce 2001). It is also intimately related to the power spectra of quadratic combinations of the temperature field and has been applied to study gravitational lensing effects (Berlareanu 1997; Zaldarriaga 2000; Hu 2001a).

The trispectrum and trispectrum quantity non-Gaussianity in harmonic space and have clear applications for secondary anisotropies. Tests for non-Gaussianity localization in angular space include the Mukowski truncations (including the genus) (Winitzki & Kosowsky 1997), the statistics of temperature extremes (Kogut et al 1996), and wavelet coefficients (Aghajani & Formi 1999). These may be more effective (Berlareanu 1997; Zaldarriaga 2000; Hu 2001a).

4.4 Non-Gaussianity

Hu & Dodelson

40

An experiment can be characterized by the data  $d$ , taken at many different times; a point-sampling matrix  $P_d$ , relating the data stream to the underlying signal at pixelized positions indexed by  $i$ ; and a noise matrix  $D_{d,n}$ , characterizing the covariance of the noise in the data stream. A model for the data then is  $d = P_d \Theta + n_d$  (with  $n_d$  being the sum over the replicating index  $i$ ); it is the sum of signal plus noise. Here  $n_d$  is drawn from a distribution (often Gaussian) with mean zero and covariance  $\langle n_d n_d^\top \rangle = C_{d,n}$ . In its simplest form the point-sampling matrix  $P_d$  is drawn from a distribution with mean  $\mu_d$  and covariance  $\Sigma_d$ , which corresponds to a particular time — with all zeroes in it except for one column with a one (see Figure 5). That column corresponds to continuous rows — which corresponds to a particular time — with all zeroes in it except for one column with a one (see Figure 5). That column corresponds to a particular pixel observed at the time of interest. Typically, a pixel will be scanned many times during an experiment, so a given column will have many ones in it, corresponding to the many times the pixel has been observed.

Figure 5 summarizes the starting point of cosmological parameters. Pre-  
of data points, to the end, the determining the path from the starting point, a time stream  
of data summarizes the starting point of cosmological parameters. Pre-  
ceding this starting point comes the calibration and the removal of systematic  
errors from the raw data, but being explicit, we do not attempt to  
cover such issues here.<sup>4</sup> Each step radically compresses the data by reducing  
the number of parameters used to describe it. Although this data pipeline and  
our discussion below are focused on temperature anisotropies, similar steps have  
been elucidated for polarization (Bunn 2001; Tegmark & de Oliveira-Costa 2001;  
Lewis et al 2001).

## 5.1 Mapmaking

That is, the noise, the difference between the data and the modulated signal, is assumed to be Gaussian with covariance  $C_d$ .  

$$C_{\theta}(d_i) = \frac{(2\pi)^{N_i/2} \sqrt{\det C_d}}{\Gamma(\frac{N_i}{2})} \exp \left[ -\frac{1}{2} (d_i - P_{\theta_i}(\Theta_i)) C_{d,i}^{-1} (d_i - P_{\theta_i}(\Theta_i))^\top \right]. \quad (26)$$
  
 There are two important theorems useful in the construction of a map and more generally in each step of the data pipeline (Telegmark et al 1997). The first is Bayes', Theorem. In this context, it says that  $P[\Theta_i|d_i]$ , the probability that the temperature is equal to  $\Theta_i$ , given the data, is proportional to the likelihood function times a prior  $P(\Theta_i)$ . Thus, with a uniform prior,

Three are two important theorems useful in the construction of a map and more generally in each step of the data pipeline (Tegmark et al 1997). The first is Bayes', Theorem. In this context, it says that  $P[\Theta_i|d_i]$ , the probability that the temperature differences are equal to  $\Theta_i$ , given the data, is proportional to the likelihood function times a prior  $P(\Theta_i)$ . Thus, with a uniform prior,

$$P[\Theta_i|d_i] \propto P[d_i|\Theta_i] \equiv L_0(\theta_i), \quad (27)$$

Aside from COBE, experiments to date have had a sizeable calibration error ( $\sim 5\text{--}10\%$ ) which must be factored into the interpretation of Planck.

That is, the noise, the difference between the data and the modulated signal, is

Given this model, a well-posed question is: what is the optimal estimator for the signal  $\Theta$ ? i.e., what is the best way to construct a map? The answer stems from the likelihood function  $\mathcal{L}$ , defined as the probability of getting the data given the theory  $\mathcal{L} \equiv P[\text{data}|\text{theory}]$ . In this case, the theory is the set of parameters

An experiment can be characterized by the data  $d$ , taken at many different times; a point-sampling matrix  $P_d$ , relating the data time-series to the underlying signal at pixelized positions indexed by  $i$ , and a noise matrix  $C_d$ , characterizing the covariance of the noise in the time-series. A model for the data then is  $d = P_d \Theta + n$ , (with  $\Theta$  implicitly sum over the repeating index  $i$ ); it is the sum of signal plus noise. Here  $n$ , is drawn from a distribution (often Gaussian) with mean zero and covariance  $\langle n_i n_j \rangle = C_{dij}$ . In its simplest form the point-sampling matrix  $P_d$  contains rows - which corresponds to a particular time - with all zeroes in it except for one column with a one (see Figure 5). That column corresponds to the particular pixel observed at the time of interest. Typically, a pixel will be scanned many times during an experiment, so a given column will have many ones in it, corresponding to the many times the pixel has been observed.

### 5.1 Mapmaking

Lewis et al. 2001).

out discussion below are focused on temperature anisotropies, similar steps have been elucidated for polarization (Bunn 2001; Tegmark & de Oliveira-Costa 2001).

cover such issues here.<sup>4</sup> Each step radically compresses the data by reducing the number of parameters used to describe it. Although this data pipeline and

Figure 5 summarizes the path from the raw data analysis starting point, a time series of data points, to the end, the determination of cosmological parameters. Preceding this starting point comes the calibration and the removal of systematic errors from the raw data, but being experimental specific, we do not attempt to

Hu & Dodson

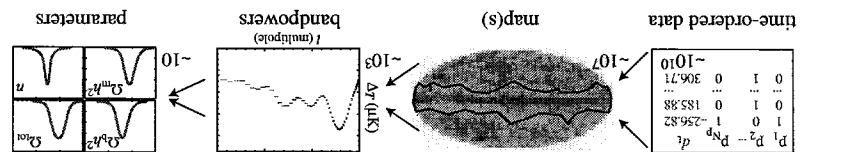
The very large CMB data sets that have begun arriving recently, innovative tools of analysis. The fundamental tool for analyzing CMB data – the likelihood function – has been used since the early days of anisotropy searches (Readehead et al 1989; Bond et al 1991; Dodelson & Jusba 1993). Brute force likelihood analysis (Tegmark & Bunn 1995) were performed even on the relatively large COBE data set, with six thousand pixels in its map. Present data sets are a factor of ten larger, and this factor will soon get larger by yet another factor of a hundred. The brute force approach, the time for which scales as the number of pixels cubed, no longer suffices.

In response, analysts have devised a host of techniques that move beyond the early brute force approach. The simplicity of CMB physics – due to linearity – is mirrored in analyses by the apparent Gaussianity of both the signal and many sources of noise. In the Gaussian limit, *optimal statistical* tests are easy to identify. These compress the data so that all of the information is retained, but they subsequently analyze – because of the compression – becomes tractable.

The Gaussianity of the CMB is not shared by other cosmological systems since gravitational non-linearities turn an initially Gaussian distribution into a non-Gaussian one. Nonetheless, many of the techniques devised to study the CMB have been proposed for studying the 3D galaxy distribution (Tegmark et al 1998), the 2D galaxy distribution (Feldman & Moody 2001; Huterer et al 2001) the Lyman alpha forest (Hu et al 2001), the shear field from weak lensing (Hu & White 2001), among others. Indeed, these techniques are now indispensable, powerful tools for all cosmologists, and we would be remiss not to at least outline them in this discussion of the CMB, the context in which many of them were developed.

5 DATA ANALYSIS

**Figure 5:** Data pipeline and radical convolutional compression. Map are constructed for each frequency channel from the data timeseries, combined and denoted of foreground contamination by a spatial (represented here by extracting the galaxy) and frequency information. Each snapshot is extracted from the maps and cosmological parameters from the bandpowers. Bandpowers are a subsampling reduction in the number of parameters needed to describe the data, from potentially  $10^{10} \rightarrow 10$  for the Planck satellite.



Hu & Dodelson

**Figure 5** indicates that the next step in the compression process is extracting bandpowers from the map. What is a bandpower and how can it be extracted from the map? To answer these questions, we must construct a new likelihood function,  $\Theta$ , but all predict the distribution from which the individual temperatures are drawn. For example, if the theory predicts Gaussian fluctuations, then  $\Theta$ , is

## 5.2 Bandpower Estimation

have different spectral shapes than the blackbody shape of the CMB. Modern experiments typically observe at several frequencies, so a well-posed question is: how can we best extract the CMB signal from the different frequency channels (Bouchet & Gisperter 1999)? The blackbody shape of the CMB relates the signal in all the channels, leaving one free parameter. Similarly, if the foreground shapes are known, each foreground comes with a free parameter per pixel. A likelihood function for the data can again be written down and the best estimator for the CMB amplitude determined analytically. While in the absence of foregrounds, one would extract the CMB signal by weighting the frequency channels according to inverse noise, when weighing the different combinations of different frequencies, we must take into account the noise in the foregrounds, which is somewhat because the foreground shapes are not precisely known, varying across the sky, e.g. from a spatially varying dust temperature. This too can be modelled in the covariance and addressed in the likelihood formalism (Tegmark 1998; White 1998). The resulting learned CMB map is obviously noisier than it foregrounds were not around, but the multiple channels keep the degradation manageable. For example, the errors on some cosmological parameters come from Planck may degrade by almost a factor of ten as compared with the no-foreground case. However, many errors will not degrade at all, and even the degraded parameters will still be determined with unprecedented precision (Knox 1999; Prunet et al 2000; Tegmark et al 2000).

$$\cdot \left\langle \frac{\partial \Theta \partial \Theta}{\Theta^2 \ln \mathcal{Z}} - \right\rangle \equiv$$

where  $C_N \equiv (\mathbf{P}^{\text{C}_1}_{\text{C}_1-1})$ . As the notation suggests, the mean of the estimator is equal to the actual  $\Theta$ , and the variance is equal to  $C_N$ . The second theorem states that this maximum likelihood estimator is also the minimum variance estimator. The Cramér-Rao inequality says no estimator can measure the  $\Theta$ , with errors smaller than the diagonal elements of  $F_{-1}$ , where the Fisher matrix is defined as

$$(28) \quad \Phi_i = C_{N,i} P_{j,i} C_{d_{i+1},d_i},$$

with the normalization constant determined by requiring the integral of the probability over all  $\Theta$ , to be equal to one. The probability on the left is the one of ability over all  $\Theta$ , to be equal to one. The probability on the right is the one of interest. The most likely values of  $\Theta$ , therefore are those which maximize the likelihood function. Since the log of the likelihood function in question, Equation (26), is quadratic in the parameters  $\Theta$ , it is straightforward to find this maximum point. Differentiating the argument of the exponential with respect to  $\Theta$ , and setting to zero leads immediately to the estimator

Although the estimator in Equation (33) represents a  $\sim 10^6$  improvement over brute force coverage of the parameter space – converging in just several iterations – it still requires operations which scale as  $N^3$ . One means of speeding up the calculations is to transform the data from the so-called signal-to-noise basis, based on an initial guess as to the signal, and throwing out those modes which have low signal-to-noise (Bond 1995; Bunn & Sugiyama 1995). The drawback is that this procedure still requires at least one  $N^3$  operation and potentially avoid this problem by iteration. Methods to potentially many as the guess at the signal improves by iteration. Methods to have been devised for experiments with particular scan strategies, but the general problem remains open. A potentially promising approach involves extracting the

In the spirit of the Newton-Raphson method, Equation (33) is used iteratively but often converges after just a handful of iterations. The usual approximation to the split of the Newton-Raphson method, Equation (33) is used iteratively but often converges after just a handful of iterations. The usual approximation to the covariation between the bands as the inverse of the Fisher matrix is then to take the covariation just a handful of iterations. The usual approximation to the covariation between the bands as the inverse of the Fisher matrix is then to take the covariation between the bands as the inverse of the Fisher matrix evaluated at the convergent point  $C_B = F_B^{-1}$ . Indeed, Tegmark (1997b) derived the identical estimator by considering all unbiased quadratic estimators, and identified this one as the one with the smallest variance.

$$F^B_{ab} = \frac{1}{2} C_{\theta^{-1}}^{jk} \frac{\partial C_{\theta^{-1}}^{ia}}{\partial \theta^{jk}} C_{\theta^{-1}}^{ib} \frac{\partial C_{\theta^{-1}}^{ja}}{\partial \theta^{ik}} . \quad (34)$$

quadratic in the data  $\Theta_i$ . The Fisher matrix is equal to

$$B^a = B^{(0)} + \frac{1}{2} f_{B,-1}^a \left( \Theta_i C_{\Theta_i, B} \partial_{\Theta_i} C_{\Theta_i, B} - C_{\Theta_i, B}^{-1} \partial_{\Theta_i} C_{\Theta_i, B} \right), \quad (33)$$

where the curvature matrix  $B_{ab}$  is the second derivative of  $-l/B$  with respect to  $B_a$  and  $B_b$ . Note the subtle distinction between the curvature matrix  $B_{ab}$  and the Fisher matrix  $F_{ab}$ , which is the inverse of the Fisher matrix in Equation (29),  $F = \langle F \rangle$ . In general, the curvature matrix depends on the data, on the  $\Theta$ . In practice, though, analysts typically use the inverse of the Fisher matrix in Equation (32). In that case, the estimator becomes

$$B^a = B_{(0)}^a + F_{-1}^{B,ab} \frac{\partial B^b}{\partial \ln L_B}, \quad (32)$$

It is clear that a "smart" sampling of the likelihood space is necessary. The numerical problem, searching for the local maximum of a function, is well-posed, and a number of search algorithms might be used.  $L_B$  tends to be sufficiently strict to let these techniques suffice. Bond et al (1998) proposed the Newton-Raphson method which has become widely used. One expands the derivative of the log of the likelihood function - which vanishes at the true maximum of  $L_B$  - around a trial point in parameter space,  $B_a^{(0)}$ . Keeping terms second order in  $B_a - B_a^{(0)}$  leads to

Hu & Dodelson

This possibility is no longer viable due to the sheer volume of data. Consider the Boomerang experiment with  $N^p = 57,000$ . A single evaluation of  $L_B$  involves computation of the inverse and determinant of the  $N^p \times N^p$  matrix  $C_0$ , both of which scale as  $N^p$ . While this single evaluation might be possible with a powerful computer, a single evaluation does not suffice. The parameter space consists of  $N^p = 19$  bandpowers equally spaced from  $l_a = 100$  up to  $l_a = 1000$ . A binning placed grid on this space would require at least ten evaluations in each dimension, so the time required to adequately evaluate the bandpowers would scale as  $10^{19} N^3$ . No computer can do this. The situation is rapidly getting worse (better) since Planck will have of order  $10^7$  pixels and be sensitive to of order  $10^3$ .

where  $C_\theta = C_S + C_N$  and  $N_p$  is the number of pixels in the map. As before,  $C_B$  is Gaussian in the antisotropic case  $\Theta$ , but in this case  $\Theta$ , are not the parameters to be determined; the theoretical parameters are the  $B_\alpha$ . Upon which the covariance matrix depends. Therefore, the likelihood function is not Gaussian in the parameter space, and there is no simple, analytic way to find the point in parameter space (which is multi-dimensional depending on the number of bands being fit) at which  $C_B$  is a maximum. An alternative is to evaluate  $C_B$  numerically at many points in a grid in parameter space. The maximum of the  $C_B$  on this grid then determines the best fit values of the parameters. Confidence levels on say  $B_1$  can be determined by finding the region within which  $\frac{d}{d\theta} [C_B - \frac{1}{2} d\theta^2] = 0.95$ .

$$\mathcal{L}_B(\Theta_i) = \frac{(2\pi)^{N/2} \sqrt{\det C_0}}{\exp\left(-\frac{1}{2}\Theta_i^T C_0^{-1} \Theta_i\right)}, \quad (31)$$

For Gaussian theories, then, the likelihood function is bands  $N_b$  probed by existing experiments.

where  $\Delta_{T,i}^2$ , depends on the theoretical parameters through  $C_i$ , (see Equation (3)). Here,  $W_i$ , the window function, is proportional to the Legendre polynomial  $P_{(n_i, n_f)}$  and a beam and pixel smearing factor  $b_2$ . For example, a Gaussian beam of width  $a$ , dictates that the observed map is actually a smoothed picture of true signal, insensitive to structure on scales smaller than  $a$ . If the pixel scale is much smaller than the beam scale,  $b_2 \propto e^{-(x/a)^2}$ . Techniques for handling asymmetric beams have also recently been developed (Wu et al 2001; Wandelt & Gorski 2001; Souradeep & Barraza 2001). Using bandpowers corresponds to assuming that  $\Delta_{T,i}^2$  is constant over a finite range, or band, of  $\ell$ , equal to  $B_i$ . For  $\ell = 6\ell_c/2 < \ell < 6\ell_c + 6\ell_c/2$ , Plate 1 gives a sense of the width and number of bands.

$$(08) \quad \text{, } \quad M^{\mu}{}_{\nu} \nabla^{\nu} \sum^{\sigma} = \langle \Theta^{\mu} \Theta^{\sigma} \rangle \equiv S^{\mu \sigma}$$

distributed as a Gaussian with mean zero and covariance equal to the sum of the noise covariance matrix  $C_N$  and the covariance due to the finite sample of the cosmic signal  $C_S$ . Inverting Equation (1) and using Equation (2) for the ensemble

In principle, one must convolve the theoretical spectrum with window functions to obtain  $B_\alpha$ , can be important. In queston of how to weight a theoretical spectrum to obtain  $B_\alpha$ , and several groups have already accounted for this fluctuation than for a downward fluctuation. The true distribution is closer to skewed: the cosmic variance of Equation (4) leads to larger errors for an upward skewness, i.e. not of the form in Equation (35). The true distribution is not Gaussian, arises since the true likelihood function for  $B_\alpha$  is not Gaussian. Another complication arises these cent experiments, DASI (Przyke et al 2001) among others have provided these cent experiments from those in Equation (30) to produce  $B_\alpha$ . Among (Knox 1999) distant with window functions (Bond et al 2000), and several groups have already accounted for this

6 DISCUSSION

Measurements of the acoustic peaks in the CMB temperature spectrum have already shown that the Universe is nearly spatially flat and began with the scale-invariant spectrum of curvature fluctuations, consistent with the simplest inflationary models. In a remarkable confirmation of a long-standing prediction of Big Bang Nucleosynthesis, the CMB measurements have now verified that barions account for about four percent of the critical density. Further, they suggest that the matter density is some ten times higher than this, implying the existence of non-baryonic dark matter and dark energy.

Future measurements of the morphology of the peaks in the temperature and polarization should determine the baryonic and dark matter content of the Universe with exquisite precision. Beyond the peaks, gravitational wave imprint on the polarization, the gravitational lensing of the CMB, and gravitational wave imprint on the early important pillars: advances in experimental technique, precision in theory, and development of data analysis techniques. The remarkable progress in the field over the last decade owes much to the efforts of researchers in all three disciplines. That much more effort will be required to fulfill the bright promise of the CMB suggests that the field will remain active and productive for years to come.

$$C_a(B_a) \approx \frac{(2\pi)^{N_a/2} \sqrt{\det C_B}}{I} \exp \left[ -\frac{1}{2} (B_a - B^*) C_B^{-1} (B_a - B^*) \right], \quad (35)$$

The huge advantage of bandpowers is that they represent the natural meeting ground of theory and experiment. The above two sections outline some of the steps involved in extracting them from the observations. Once they are extracted, any theory can be compared with the observations without knowledge of experimental details. The simplest way to estimate the cosmological parameters in a set  $\mathcal{C}$ , is to approximate the likelihood as

### 5.3 Cosmological Parameter Estimation

real space correlation functions as an intermediate step between the map and the bandpowers (Szapudi et al 2001). Another involves consistently analyzing coarsely pixelized maps with highly detailed sub-maps (Dore et al 2001).

$$F_{c,ii} = \frac{\partial c_i}{\partial B_a} C_{B,-1}^{B,a} \frac{\partial c_j}{\partial B_b}. \quad (36)$$

In the approximation that the band power covariance  $C_B$  is independent of the parameters  $\zeta$ , maximizing the likelihood is the same as minimizing  $\chi^2$ . This has been done by dozens of groups over the last few years especially since the release of CMBFAST (Seljak & Zaldarriaga 1996), which allows fast computation of theoretical spectra. Even after all the computation summarized in Figure 5, these analyses are still computationally cumbersome due to the large numbers of parameters varied. Various methods of speeding up spectra computation have been proposed (Tegmark & Zaldarriaga 2000), based on the understanding of the physics of peaks outlined in §3, and Monte Carlo explorations of the likelihood function (Christensen et al 2001).

was supported by NASA NAG-5-10840 and the DOE OJI Program. S.D. was supported by the DOE, by NASA grant NAG-5-10842 at Fermilab, by NSF Grant PHY-0079251 at Chicago.

## ACKNOWLEDGMENTS

Future measurements of the morphology of the peaks in the temperature and polarization should determine the baryonic and dark matter content of the Universe with exquisite precision. Beyond the peaks, gravitational wave imprint on the polarization, the gravitational lensing of the CMB, and gravitational scattering secondary anisotropies hold the promise of understanding the physics of inflation and the impact of dark energy on structure formation.

In fact, this estimate has been widely used to forecast the optimal errors on cosmological parameters given a proposed experiment and a band covariance matrix  $C_B$ , which includes diagonal sample and instrumental noise variance. The reader should be aware that no experiment to date has even come close to achieving the precision implied by such a forecast!

Hu & Dodelson

## Literature Cited

CMB Anisotropies

